

An enhanced PIRATA data set for tropical Atlantic ocean-atmosphere research

Gregory R. Foltz¹, Claudia Schmid¹, and Rick Lumpkin¹

¹NOAA/Atlantic Oceanographic and Meteorological Laboratory, Miami, FL USA

Corresponding author: gregory.foltz@noaa.gov

Revised for *Journal of Climate*

15 November 2017

Abstract

The Prediction and Research Moored Array in the Tropical Atlantic (PIRATA) provides measurements of the upper ocean and near-surface atmosphere at 18 locations. Time series from many moorings are nearly 20 years in length. However, instrumental biases, data drop-outs, and the coarse vertical resolutions of the oceanic measurements complicate their use for research. Here an enhanced PIRATA data set (ePIRATA) is presented for the 17 PIRATA moorings with record lengths of at least seven years. Data in ePIRATA are corrected for instrumental biases, temporal gaps are filled using supplementary data sets, and the subsurface temperature and salinity time series are mapped to a uniform 5-m vertical grid. All original PIRATA data that pass quality control and do not require bias correction are retained without modification, and detailed error estimates are provided. The terms in the mixed layer heat and temperature budgets are calculated and included, with error bars. As an example of ePIRATA's application, the vertical exchange of heat at the base of the mixed layer (Q_{-h}) is calculated at each PIRATA location as the difference between the heat storage rate and sum of net surface heat flux and horizontal advection. Off-equatorial locations are found to have annual mean cooling rates of 20–60 W m⁻², while cooling at equatorial locations reaches 85–110 W m⁻² between 10°W–35°W and decreases to 40 W m⁻² at 0°. At most off-equatorial locations, the strongest seasonal cooling from Q_{-h} occurs when winds are weak. Possible explanations are discussed, including the importance of seasonal modulations of mixed layer depth and the diurnal cycle.

1 Introduction

The tropical Atlantic has a strong seasonal cycle that is shaped by coupled ocean-atmosphere-land interactions (Mitchell and Wallace 1992, Okumura and Xie 2004). Deviations of sea surface temperature (SST) and winds from the seasonal cycle, though less pronounced than seasonal changes, are important because of their influence on the location of the Intertropical Convergence Zone (ITCZ) (Nobre and Shukla 1996, Chiang et al. 2002), continental rainfall (Nobre and Shukla 1996, Polo et al. 2008, Yoon and Zeng 2010), and anomalous SST and atmospheric circulation in other ocean basins (Kucharski et al. 2007, Rodriguez-Fonseca et al. 2009, Ham et al. 2013).

The Prediction and Research Moored Array in the Tropical Atlantic (PIRATA) was established in 1997 to improve our understanding and predictability of tropical Atlantic weather and climate (Servain et al. 1998, Bourlès et al. 2008). The array was designed to sample the two main patterns of interannual-decadal variability: the Atlantic Meridional Mode (Nobre and Shukla 1996, Chiang and Vimont 2004) and the Atlantic equatorial mode (Zebiak 1993, Carton and Huang 1994). Three moorings were added to PIRATA in 2005 as the Southwest Extension, followed by four additional Northeast Extension moorings in 2006–2007, and a Southeast Extension mooring at 6°S, 8°E that was first deployed during 2006–07 (Rouault et al. 2009) and then from 2013 to the present (Figure 1). Scientific motivation for these extensions includes the connection between tropical Atlantic SST and hurricane activity (Kossin and Vimont 2007), the potential impact of the salinity-induced barrier layer on hurricanes and tropical Atlantic climate (Breugem et al. 2008, Reul et al. 2014), the importance of South Atlantic SSTs for South American rainfall variability (Bombardi et al. 2014), and persistent coupled climate model biases (Richter and Xie 2008).

Measurements from PIRATA have been used to address a variety of research topics, including the Equatorial Undercurrent, upper-ocean diurnal cycle, and tropical instability waves at 0° , 23°W (e.g., Grodsky et al. 2005, Giarolla et al. 2005, Wenegrat and McPhaden 2015), carbon parameters and the factors affecting CO_2 variability at 6°S , 10°W (e.g., Parard et al. 2014, Lefèvre et al. 2016), seasonal variations of salinity and their potential impact on SST (e.g., Foltz and McPhaden 2009, Foltz et al. 2015), and the causes of seasonal and interannual variations of SST (e.g., Foltz et al. 2003, 2012, 2013a, Rugg et al. 2016). PIRATA data have also been used to validate satellite-based measurements of SST (Gentemann et al. 2004), rainfall (Serra and McPhaden 2003), and winds (Ebuchi et al. 2002), and for validation of numerical model output and atmospheric and oceanic reanalyses (e.g., Han et al. 2008, Wade et al. 2011, Nobre et al. 2012).

The time series from many PIRATA moorings are approaching 20 years in length and are a valuable resource for examining upper-ocean and near-surface atmospheric variability on diurnal to decadal timescales. The moorings' sensors are calibrated after every buoy recovery (approximately once per year) and regularly quality-controlled, yet instrumental biases can remain, and there are some gaps in the time series due to sensor failure or other unforeseen circumstances (Figure 1 and Appendix; see <http://www.pmel.noaa.gov/tao/drupal/disdel/> for full details of data availability). In addition, the vertical resolutions of the subsurface temperature and salinity measurements from the moorings are often too coarse to resolve fully the mixed layer depth and vertical salinity structure, key parameters that affect ocean-atmosphere variability. Since the first PIRATA moorings were deployed in 1997, many new satellite, reanalysis, and in situ data sets have become available (e.g., Argo, ERA-interim reanalysis, microwave

70 SST, satellite sea surface salinity) that can be used to fill gaps in PIRATA time series
71 and to provide enhanced vertical resolution of PIRATA temperature and salinity data.

72 In the remainder of the paper we describe a new “enhanced” PIRATA data
73 set (ePIRATA) that provides rigorously quality-controlled, gap-filled (temporal and
74 vertical) time series for ocean-atmosphere research and model validation in the tropical
75 Atlantic. ePIRATA complements the tropical Atlantic components of global data sets
76 such as TropFlux (Kumar et al. 2012), OAFlux (Yu and Weller 2007), Argo ([www.argo.](http://www.argo.ucsd.edu/Gridded_fields.html)
77 [ucsd.edu/Gridded_fields.html](http://www.argo.ucsd.edu/Gridded_fields.html)), and the Ocean Surface Current Analysis Realtime
78 (OSCAR; Bonjean and Lagerloef 2002), which use in situ measurements from moorings
79 only for validation or to adjust satellite and reanalysis data for biases. Here, in contrast,
80 we retain all original mooring data after quality-control and fill gaps with other in
81 situ data and bias-corrected satellite and reanalysis products, forming high-quality
82 continuous daily records, with error bars, at each of the 17 PIRATA locations with
83 a record length of at least seven years. Also included in ePIRATA are continuous
84 daily time series of terms in the mixed layer heat and temperature budgets at each
85 mooring location, which we anticipate will be useful for exploring the mechanisms
86 of SST variability and the causes of biases in climate models. After describing the
87 methods used to create ePIRATA, we use the data set to calculate the mixed layer
88 heat budget residuals at the mooring locations and relate them to annual mean and
89 seasonal variations of vertical turbulent cooling at the base of the mixed layer.

90 **2 Data and Methods**

91 In this section we describe the data and methods used to create ePIRATA, beginning
92 with the atmospheric parameters and followed by the oceanic data. All moorings mea-

93 sure subsurface temperature and conductivity (used to calculate salinity), as well as air
94 temperature, relative humidity, shortwave radiation, winds, and rainfall. Several moor-
95 ings also measure barometric pressure, downward longwave radiation, and ocean veloc-
96 ity at a depth of 10 m (Table 1). All data except rainfall and barometric pressure are
97 used in this study. We exclude these variables because they are not used directly to cal-
98 culate the mixed layer heat and temperature budgets, one of the main motivations for
99 ePIRATA. Additionally, because of the short timescales and small spatial scales associ-
100 ated with tropical rainfall, filling gaps with gridded data sets is more challenging (Serra
101 and McPhaden 2003). All PIRATA data used in this study are the daily averages, avail-
102 able in real-time from www.pmel.noaa.gov/tao/disdel/frames/main.html. Higher
103 temporal resolution data are also available from the moorings, but they are not avail-
104 able in real-time and sometimes not for several years following a deployment. For
105 this reason, and because the coarse vertical resolutions of temperature and salinity on
106 many moorings cannot resolve well the diurnal cycle, we use only the daily-averaged
107 data. Note that any corrections applied to the high-resolution delayed-mode data after
108 post-recovery calibration have also been applied to the daily-averaged data.

109 **2.1 Atmospheric Data**

110 As mentioned in the previous section, biases can develop in the PIRATA time series
111 during approximately year-long buoy deployments. The first steps are therefore to
112 remove data that are obviously biased and fill temporal gaps in the records.

113 **2.1.1 Air Temperature, Relative Humidity, and Winds**

114 To determine the quality of the air temperature data, we first create a daily climatology
115 of the difference between SST and air temperature (ΔT) using all available data from

116 a given mooring. We also compute the daily standard deviation of ΔT with respect
 117 to its climatology. Because biases very rarely develop in ocean temperature measure-
 118 ments (Freitag et al. 1999), most biases in ΔT can be attributed to issues with the air
 119 temperature sensors. The advantage of using ΔT instead of air temperature itself is
 120 that ΔT exhibits much smaller variability outside of the seasonal cycle than air tem-
 121 perature. For example, there are noticeable interannual variations in air temperature
 122 at many locations, but interannual variations in ΔT are much smaller (Figure 2a).
 123 We focus on identifying data with a spurious long-term drift over at least one month
 124 because (1) this is the dominant source of error and (2) biases in shorter-frequency
 125 variability are very difficult to detect.

126 First, for each day at a given location, we count the number of days in a centered
 127 31-day window that have ΔT less than the daily climatology minus one standard devi-
 128 ation (N_l) or greater than the climatology plus one standard deviation (N_h). A period
 129 of 31 days was chosen to focus on removing spurious drifts that last longer than one
 130 month. Next, the 0.15 and 0.85 quantiles of N_h and N_l are calculated for each calendar
 131 day (Q_{15} and Q_{85} , respectively), and days when $N_h > Q_{85}$ or $N_l < Q_{15}$ are flagged as
 132 periods when there may be biases in the air temperature measurements. Finally, for a
 133 101-day moving window centered on each day, if the number of days with low flags or
 134 high flags is greater than 50, the flagged values are removed from the record. This step
 135 is then repeated with a 301-day moving window and a threshold of 90 days instead of
 136 50. We found, after experimentation, that using a 101-day window with a threshold
 137 of 50 gave reasonably robust identification of obviously biased air temperature data.
 138 Using fewer days resulting in the elimination of too much data because of some periods
 139 with large high-frequency fluctuations of the air-sea temperature difference. Also, due

140 to natural high-frequency variations of the temperature difference, it is necessary to
141 use a longer period of 301 days to identify biases that are small at first and become
142 larger over several months.

143 This procedure results in up to 5% of the data being removed at each location.
144 Additional subjective quality control is performed based on the ΔT time series, result-
145 ing in the total removal of up to 35% of the data at a given location. The subjective
146 procedure mainly involves identifying whole buoy deployments, typically 1–2 years in
147 length, with questionable data that were not entirely removed by the objective method.
148 As an example, the 0°, 35°W mooring record contains highly questionable data during
149 the late 2006 to early 2008 deployment and the early 2009 to mid 2010 deployment
150 (Figure 2a). All of these data were removed, regardless of whether they were flagged
151 by the objective method. Removal was motivated mainly by the presence of sustained
152 negative ΔT values, which were not observed except during these deployments. It is
153 unclear what causes these biases during some deployments, especially since instrumen-
154 tal errors are only about 0.2°C based on pre-deployment and post-recovery calibration
155 coefficients (Lake et al. 2003). It is possible that something became stuck on the
156 temperature sensor while deployed on the buoy, reducing air flow and hence increasing
157 the temperature the sensor recorded.

158 To verify that periods of several months with air temperature greater than
159 SST are unrealistic, we calculated the monthly air-sea temperature difference at each
160 PIRATA location from the International Comprehensive Ocean-Atmosphere Dataset
161 (ICOADS; Woodruff et al. 2011) during 1960–2007. We found that 0–0.7% of the
162 months at each location have air temperature greater than SST for that month and
163 the following four months. In the monthly TropFlux data set, during 1979–2015 at each

location there are at most three months total, and at most two consecutive months, with air temperature greater than SST, and differences are always less than 0.1°C . The questionable values of air temperature that we remove from PIRATA records are well outside of these bounds in terms of magnitude and duration.

The same procedure is used to quality-control the relative humidity time series from the moorings, except the climatological value is subtracted from the observations to derive the daily anomalies that are used for the detection of biases. This approach results in the removal of up to 5% of the data at each location, except 15% at 0°N , 35°W (Figure 2b). No data were removed from the PIRATA wind records because no obviously biased values were found. Any remaining gaps in the mooring air temperature, relative humidity, and wind time series were filled with the mooring climatology plus daily ERA-interim reanalysis (Dee et al. 2011) anomalies. The mooring and ERA-interim climatologies were calculated using the same time periods. Kumar et al. (2012) found that ERA-interim near-surface air temperature, humidity, and winds generally agree best with mooring values compared to other reanalysis products. Detailed comparisons at each PIRATA location are provided in the Appendix. We use only ERA-interim anomalies from the seasonal cycle in order to eliminate possible annual mean and seasonally varying biases. Note that ERA-interim does not assimilate PIRATA measurements.

2.1.2 Shortwave and Longwave Radiation

The main source of error in PIRATA shortwave radiation measurements is the buildup of dust and other aerosols on the radiometer domes at buoy locations north of 4°N (Foltz et al. 2013b). These time-dependent biases are removed following the “MERRA clear-sky” method described in Foltz et al. (2013b). Gaps in the time series are

188 filled following the methodology of Kumar et al. (2012) as follows. For each buoy
 189 time series, we first form a daily climatology. We then regress daily NOAA satellite
 190 outgoing longwave radiation (OLR) anomalies at the buoy location onto the bias-
 191 corrected PIRATA shortwave anomalies. The regression coefficients are applied to the
 192 time series of OLR anomalies to create an OLR-based shortwave radiation anomaly
 193 time series that is used to fill gaps in the PIRATA time series. The method works
 194 reasonably well in the regions where high cloudiness dominates (south of 20°N and
 195 outside of the cold tongue region), with daily and monthly anomaly correlations of 0.5–
 196 0.8 between the PIRATA shortwave radiation and the OLR-regressed values (Figure
 197 3). In regions where low cloudiness is more important (e.g., 20°N, 38°W, the eastern
 198 equatorial Atlantic, and 6°S and 10°S along 10°W), correlations are generally lower
 199 (0.3–0.4). Note that these correlations are for anomalies from the mean seasonal cycle
 200 and that correlations between the full time series range from 0.67 to 0.92, as described
 201 in the Appendix.

202 Downward longwave radiation is recorded on six PIRATA buoys (Table 1). At
 203 four locations with long records that are unbiased by dust (indicated in Table 1),
 204 downward radiation from the moorings is used, and gaps are filled with the daily
 205 PIRATA climatology plus the ERA-interim daily anomalies. At these locations, the
 206 correlations between daily anomalies of PIRATA and ERA-interim downward longwave
 207 radiation are between 0.43 (at 10°S, 10°W) and 0.66 (at 19°W, 34°W). Full correlations
 208 and RMS differences, calculated with data that include the seasonal cycle, are shown
 209 in the Appendix. At all other locations, downward longwave radiation directly from
 210 ERA-interim is used. Outgoing surface longwave radiation is calculated as $\epsilon\sigma T^4$, where
 211 $\epsilon = 0.97$, σ the Stefan-Boltzman constant, and T is SST from the gap-filled PIRATA

record (the methodology used to fill gaps is described in the next section).

2.2 Oceanic Data

The oceanic measurements from the PIRATA moorings consist of temperature, salinity, and velocity. At all locations, temperature is available at depths of 1 m and 20 m, at 20 m intervals down to 140 m, and at 180 m, 300 m, and 500 m. Many moorings have additional sensors in the upper 40 m. Salinity is available at 1 m, 20 m, 40 m, and 120 m at all moorings, and many have additional measurements in that depth range. Velocity is available from some moorings at a depth of 10 m (Table 1 shows the locations). In this section we describe the methodologies used to remove questionable PIRATA data, fill temporal gaps, and perform vertical interpolation.

2.2.1 Temperature and Salinity

We found no obvious biases in the mooring temperature and velocity time series, based on comparisons between mooring and satellite SST data and examination of the PIRATA time series for discontinuous jumps or suspicious linear trends during deployments, so no data were removed from them. Gentemann et al. (2004) also did not find any obviously biased SST mooring data in their comparison to microwave SST. For salinity, instrumental bias is most easily detected by examining time series of differences in salinity between depth levels. The first step in the quality-control procedure is therefore calculating differences between the PIRATA salinity from all available depth pairs (ΔS) for every day in a given record. The full set of depth pairs includes all pairs of unique depths, using only the depths at which salinity measurements are available. For example, on a given day if salinity is available at depths of 1, 20, 40, and 120 m, there are six depth pairs ([1,20], [1,40], [1,120], [20,40], [20,120], [40,120]). The

235 available depths and depth pairs can be different on different days because of missing
236 data and occasionally the deployment of new sensors during a servicing cruise. From
237 these ΔS values, three-month seasonal means (January–March, etc.) and standard
238 deviations are calculated for each depth pair. These are used to test whether data on
239 a given day for a given pair of depths are questionable. As before, a moving 31-day
240 window centered on each day in a given PIRATA record is used. If all 31 values of ΔS
241 for a given depth pair exceed the seasonal mean plus three standard deviations, or are
242 lower than the seasonal mean minus three standard deviations, the 31 values at each
243 depth level are flagged. This procedure is repeated for all depth pairs. The flagged
244 data are examined and obviously biased measurements are discarded.

245 The most obvious indicator of erroneous data is a near-surface salinity inversion
246 (i.e., values that decrease with depth) that is not supported by strong temperature
247 stratification, or surface salinity that is abnormally fresher than salinity at a deeper
248 level for an extended period of time. As examples, instances of salinity inversions
249 were found at 12°N, 38°W during 2004 and 2008–09, at 0°, 0° during 2012–2013, and
250 at 10°S, 10°W during early 2011 (Figure 4). Periods with abnormally low salinity
251 at 1 m compared to 20 m were also found at 12°N, 38°W during late 2007 and at
252 10°S, 10°W during 2008 and 2013–14 (Figure 4a,c). In many cases, it is easy to label
253 the abnormally fresh values as erroneous because the fresh bias with respect to the
254 next depth immediately disappears when the mooring is serviced and new sensors are
255 installed. Such servicing occurred in April 2008 at 12°N, 38°W (Figure 4a) and in
256 September 2008 at 10°S, 10°W (Figure 4c). Overall, this quality-control procedure
257 results in the removal of up to 6% of the salinity data at each location. Resulting gaps
258 in PIRATA surface salinity after July 2011 are filled using the daily climatology from

the mooring plus daily anomalies from the Aquarius satellite instrument. This method works reasonably well at most locations (see Appendix for more details). Aquarius data are available from <http://podaac.jpl.nasa.gov/aquarius> beginning in August 2011 and continuing through May 2015. We anticipate that surface salinity from the Soil Moisture and Ocean Salinity (SMOS) satellite sensor will be useful for filling gaps in future updates to ePIRATA. Gaps in PIRATA SST are filled with microwave satellite SST, available starting in 1998 from <http://www.remss.com/measurements/sea-surface-temperature/oisst-description>, using a similar methodology.

Next, historical Argo profiles are used to map each daily PIRATA temperature and salinity profile to a uniform 5 m resolution in depth. We first obtain all Argo temperature and salinity profiles within $\pm 2^\circ$ of latitude and $\pm 3^\circ$ of longitude of a given PIRATA mooring, and within ± 90 days of a given calendar day. For example, for April 1, 2010, all profiles available during January–June of any year are obtained. We then interpolate each Argo profile to a 5 m vertical grid, from 10 m to 200 m, and extend it upward to 5 m and 1 m using the value at 10 m. The assumption of a uniform layer from 1 m to 10 m is reasonable because we are using daily-averaged PIRATA data. There are between 390 and 1605 profiles available for the regression at each PIRATA location. The fewest are available at the Southwest Extension sites and at 0° , 35°W , and the largest numbers are found along 23°W and at 20°N , 38°W . For each day in a PIRATA record with temperature available at a minimum of two levels, we first identify all missing levels, defined as depths of 1 m, and from 5 m to 200 m in 5 m increments, that do not have PIRATA data on that day. For each missing depth, we obtain temperature at that depth from all Argo profiles in the ± 90 day time-span and $2^\circ \times 3^\circ$ region surrounding the mooring. We then obtain all Argo temperature data

at the depths for which PIRATA temperature is available and perform multiple linear regression of the Argo temperatures at the available depths onto Argo temperatures at the missing depth. Using the resultant regression coefficients, we estimate the PIRATA temperature at the missing depth on the given day as

$$T_m = a_0 + \sum_{i=1}^A a_i T(z_i) \quad (1)$$

Here a_0 and a_i are the regression coefficients that convert PIRATA temperatures at the available depths ($T(z_i)$) to temperature at the missing depth (T_m), and A is the number of depths for which PIRATA temperature is available on the given day. The Argo regression and (1) are repeated for each missing PIRATA depth on the given day, and then repeated for all days in a given PIRATA record. The result is a profile of temperature between 1 m and 200 m at a 5 m vertical resolution on each day for which PIRATA temperature is available at a minimum of two depth levels. The same methodology is used for salinity, except Argo temperature and salinity profiles are used in the regression model because we found that the inclusion of temperature improves the model.

This method significantly reduces biases that result from simple linear interpolation between the nearest PIRATA depth levels and gives small reductions in RMS error relative to linear interpolation (Figures 5, 6). For this comparison, we first retained Argo temperature data only at 20 m intervals between 20 m and 140 m, and at 180 m, and salinity only at 20, 40, and 120 m. These are depths at which data are typically available at all moorings. The moorings also measure temperature and salinity at a depth of 1 m. Because Argo measurements are generally not available at 1 m, temperature and salinity at 10 m were used to represent values at a depth of 1 m.

307 We then used 75% of the Argo data at each location to “train” the regression model
308 and filled gaps in the remaining 25% of the profiles using the regression coefficients and
309 the data at the available depths, based on (1). Note that in general these are not the
310 exact errors associated with mapping the actual PIRATA data to a 5 m vertical grid,
311 which depend on the depths at which PIRATA temperature is available on a given day,
312 the specific mooring location, and to a lesser extent, the time of year. The calculation
313 of these errors is described in the Appendix.

314 Though the Argo regression method reduces biases introduced by the use of sim-
315 ple linear interpolation in depth, it occasionally generates unrealistic vertical gradients
316 of temperature or salinity for cases in which the regression model has low predictabil-
317 ity. To eliminate unrealistic temperature values, we first determine the maximum and
318 minimum observed vertical temperature gradient over a distance of 5 m (i.e., between
319 two vertical grid points), based on all Argo profiles within 2° of latitude and 3° of
320 longitude of the mooring and for a given calendar month. If the vertical gradient for
321 any ePIRATA daily-averaged profile, calculated between two depth levels, is outside of
322 these upper and lower bounds set for each calendar month, temperature at each depth
323 level is removed and filled using the climatology (based on all data available at that
324 depth) plus the anomaly vertically interpolated between the closest available depths
325 with good data. However, if original PIRATA data are available at a given depth, they
326 are retained. The procedure is then repeated using gradients over a distance of 20 m.
327 The same method is used to eliminate unrealistic salinity data. This results in the
328 replacement of up to 5% of the temperature and salinity data at most locations.

329 When PIRATA temperature or salinity data are available at zero or one depth
330 level, different techniques are used to fill the gaps. These gaps can occur, for example,

331 if the mooring line breaks and instruments are not recovered. If the temporal gap
 332 at a given level is 10 days or less, linear interpolation in time is performed at that
 333 depth. If the gap is longer than 10 days, optimum interpolation is performed, using
 334 all Argo profiles within $\pm 10^\circ$ of latitude, $\pm 15^\circ$ of longitude, and ± 3 months from a
 335 given mooring on a given day. The cut-off of 10 days was chosen because we found
 336 that linear interpolation outperforms optimum interpolation at each location when the
 337 gap is less than about 10 days, and optimum interpolation is better for filling longer
 338 gaps. In practice, linear interpolation is rarely used, however, since less than 1% of
 339 the days at each location are part of a temperature or salinity gap that is 10 days or
 340 less. Optimum interpolation is more commonly performed, since as many as 44% of
 341 the days at some locations are part of gap that is longer than 10 days.

342 Following Reynolds and Smith (1994) and Kawai et al. (2006), optimum inter-
 343 polation can be expressed as

$$344 \quad A_k = F_k + \sum_{i=1}^N w_{ki}(T_i - F_i) \quad (2)$$

346 Here A_k is the interpolated “analysis” value for a given PIRATA location, day, and
 347 depth, F_k is the monthly climatological first-guess value from World Ocean Atlas 2013
 348 (WOA13; Locarnini et al. 2013, Zweng et al. 2013), linearly interpolated to the PI-
 349 RATA location, calendar day, and depth, T_i and F_i are the individual Argo observations
 350 and associated WOA13 first-guess values, respectively, at location-time i , and N is the
 351 total number of Argo profiles within the latitude, longitude, and time ranges specified
 352 previously. The weights (w_{ki} in (2)) can be expressed as

$$353 \quad \Pi_{ki} = \sum_{j=1}^N w_{kj} \Pi_{ij} \quad (3)$$

where Π_{ki} is the correlation between the first-guess error at the mooring location and the error for a given Argo measurement and Π_{ij} is the correlation between the first-guess errors associated with two given Argo measurements. We have assumed that the observational errors from individual Argo measurements are uncorrelated, and we use a Gaussian function in space and time for both sets of correlation coefficients, following Reynolds and Smith (1994):

$$\Pi_{ij} = \exp \left[- \left(\frac{x_i - x_j}{L_x} \right)^2 - \left(\frac{y_i - y_j}{L_y} \right)^2 - \left(\frac{t_i - t_j}{L_t} \right)^2 \right] \quad (4)$$

Decorrelation scales are set to $L_x = 300$ km, $L_y = 200$ km, and $L_t = 15$ days, and the results are not very sensitive to other reasonable choices of these parameters. The percentage of depth levels filled with Argo optimal interpolation is up to 44% for salinity and up to 28% for temperature, depending on the gaps present in each PIRATA time series.

The resulting time series are then checked for static stability using the method of Jackett and McDougall (1995). If there is instability at a given depth, we determine whether it is caused by temperature, salinity, or both by performing the stability calculation again using constant salinity as a function of depth, then using constant temperature. Unstable temperature and salinity values are replaced with the climatology plus the anomaly linearly interpolated between the closest depths with stable values. If there are still instabilities, the unstable values are replaced using linear interpolation in depth. Original PIRATA temperature and salinity data, with the exception of those removed using the methodology described earlier in this section, are retained regardless of the stability. Therefore, the result of the interpolation and stability-checks is continuous daily time series of temperature and salinity at each PI-

379 RATA location, with 5 m vertical resolution, in which all original PIRATA data that
380 pass quality-control have been retained.

381 **2.2.2 Mixed Layer Depth and SST gradients**

382 The mixed layer depth (MLD) can be defined as the depth at which density is $\Delta\rho$
383 greater than the density at a depth of 1 m. Using the ePIRATA temperature and
384 salinity, we choose a value of $\Delta\rho$ that is a balance between (1) maximizing the seasonal
385 amplitude of MLD (periods greater than 180 days) relative to smaller timescale vari-
386 ability (standard deviation of MLD high-pass filtered at a period of 10 days) and (2)
387 minimizing the difference between SST and temperature averaged in the mixed layer
388 (T). The reasoning behind (1) is that it is desirable to have a MLD with a well-defined
389 seasonal cycle and which is not strongly influenced by spurious higher-frequency varia-
390 tions induced by uncertainties in the vertical interpolation of temperature and salinity.
391 We choose a 10-day cut-off period for high-frequency variations so that intraseasonal
392 variability is excluded, though results are not very sensitive to the period chosen. Sim-
393 ilar arguments were used by de Boyer Montégut et al. (2004), though they calculated
394 MLD over the global ocean. In general, larger $\Delta\rho$ give stronger seasonal cycles of MLD
395 and weaker high-frequency variations. The reason for (2) is that this requirement is
396 advantageous for relating the terms in the mixed layer heat and temperature budgets
397 to changes in SST. For larger $\Delta\rho$ (increasing from zero to 0.3 kg m^{-3}), the MLD, its
398 seasonal amplitude, and the ratio of the seasonal amplitude to high-frequency vari-
399 ability all increase when averaged across all mooring locations (Figure 7a). However,
400 the difference between SST and T also increases, as does the seasonal amplitude of
401 $SST - T$ (Figure 7b). Based on these considerations, we define the MLD as the depth
402 at which density is 0.12 kg m^{-3} greater than at 1 m. This definition results in a mean

403 $SST - T$ of 0.06°C (black square in Figure 7b) and a seasonal cycle of MLD that is four
 404 times larger than the amplitude of high-frequency variability (purple square in Figure
 405 7a). Our density criterion translates to a temperature criterion of about 0.35°C , which
 406 is similar to that chosen by de Boyer Montégut et al. (2004), considering that they
 407 used a reference depth of 10 m instead of our 1-m depth.

408 We use daily microwave SST to estimate horizontal mixed layer temperature
 409 gradients, which are needed along with mixed layer depth and velocity to calculate
 410 horizontal temperature and heat advection, important terms in the mixed layer tem-
 411 perature and heat budgets, respectively. The horizontal SST gradients are provided as
 412 part of the ePIRATA data set. To determine the optimal spatial averaging to apply
 413 to the $\frac{1}{4}^{\circ}$ satellite SST data before computing gradients, we compared the RMS dif-
 414 ferences between daily satellite SST at each PIRATA location, using different spatial
 415 averaging, to daily SST from the mooring. We considered spatial averaging regions
 416 centered on the mooring location and ranging from $0.25^{\circ} \times 0.25^{\circ}$ to $1.75^{\circ} \times 1.75^{\circ}$.
 417 The minimum RMS difference, averaged across all PIRATA locations, was found for a
 418 $1^{\circ} \times 1^{\circ}$ average. The RMS difference tends to be larger for smaller averaging regions
 419 because of a smaller signal to noise ratio and increases for regions larger than $1^{\circ} \times 1^{\circ}$
 420 because the averaged SST is less representative of the mooring SST. We therefore use
 421 centered differences of $1^{\circ} \times 1^{\circ}$ averages of satellite SST, calculated over a distance of one
 422 degree, to calculate horizontal SST gradients at each PIRATA location. For example,
 423 for zonal gradients at 0° , 35°W , SST is first averaged in 1° boxes centered at 35.5°W
 424 and 34.5°W , then the difference between these spatial averages is calculated.

425 2.2.3 Velocity

426 At the off-equatorial locations with velocity measurements (see Table 1), we use the
427 mooring data without correction and fill temporal gaps with a weekly surface drifter-
428 altimetry-wind synthesis product (Lumpkin and Garzoli 2011) linearly interpolated
429 to a daily time series at each mooring location. Daily anomalies from the seasonal
430 cycle are added to the daily climatology calculated using all available PIRATA data
431 at a given mooring. Comparisons between the mooring velocity time series and those
432 from the drifter product and OSCAR revealed that the drifter product compares more
433 favorably at most locations in terms of annual mean and seasonal amplitude of zonal
434 and meridional velocity. At 0° , 23°W we fill gaps with OSCAR since the drifter product
435 relies on Ekman balance for the wind-driven component and is therefore unavailable
436 on the equator. At other equatorial locations, where no velocity data is available from
437 the moorings, we also use OSCAR. The RMS differences and correlations between
438 PIRATA 10-m velocity and the products used to fill gaps are shown in the Appendix.

439 To convert the continuous records of 10 m velocity at each mooring location to
440 vertically-averaged velocity in the mixed layer (needed for the calculations of horizontal
441 mixed layer heat and temperature advection, and included in the ePIRATA data set),
442 we use monthly Ocean Reanalysis System 4 (ORAS4) data for 2000–2014 (Balmaseda
443 et al. 2013). In general, we found that ORAS4 velocity compares more favorably to
444 PIRATA than the Simple Ocean Data Assimilation (SODA), Global Ocean Data As-
445 simulation (GODAS), or Estimating the Circulation and Climate of the Ocean (ECCO)
446 products. This may be due in part to the assimilation of PIRATA temperature and
447 salinity measurements in ORAS4. For the zonal and meridional components sepa-
448 rately, we regress the ORAS4 mixed layer velocity onto the 10 m velocity and MLD.

449 The multiple linear regression is performed at each PIRATA location, and the resulting
 450 coefficients are used along with daily MLD from the mooring location to adjust the 10 m
 451 velocity to mixed layer-averaged velocity. The result of the correction is a mixed layer
 452 velocity with a stronger eastward component at most locations. Record-length mean
 453 differences between mixed layer and 10 m zonal velocity are -0.3 to 3.7 cm s⁻¹ except
 454 at 0°, 23°W and 0°, 35°W, where the mean differences are 8.1 and 12.9 cm s⁻¹ due to
 455 deep mixed layers and a strong Equatorial Undercurrent. There is a strong seasonality
 456 to the corrections along the equator, with the largest values during July–January, when
 457 the mixed layer is thickest (Figure 8a). Mean corrections and seasonality are generally
 458 much weaker at the off-equatorial sites (Figure 8b). Corrections to meridional velocity
 459 are -3.1 to 1.7 cm s⁻¹ and are northward (>0) only at the Southern Hemisphere sites,
 460 reflecting the dominance of the poleward Ekman component, which is strongest at the
 461 surface.

462 **2.3 Mixed Layer Heat and Temperature Budgets**

463 Mixed layer heat and temperature budget analyses are useful techniques for assessing
 464 the causes of changes in mixed layer heat content and SST, respectively. The heat
 465 budget equation can be expressed as

$$466 \rho c_p h \frac{\partial T}{\partial t} = -\rho c_p h \mathbf{v} \cdot \nabla T + Q_0 + Q_{-h} \quad (5)$$

468 Here h is the mixed layer depth, T is vertically averaged temperature in the mixed layer,
 469 \mathbf{v} is horizontal velocity averaged in the mixed layer, ∇T is the horizontal gradient of T ,
 470 estimated using satellite SST, Q_0 is the net surface heat flux, consisting of shortwave
 471 radiation absorbed in the mixed layer, net surface longwave radiation absorption, and

472 latent and sensible heat fluxes, and Q_{-h} is the vertical turbulent flux of heat at the
 473 base of the mixed layer. The mixed layer temperature equation is simply equation
 474 (5) divided by $\rho c_p h$. We use the ePIRATA daily time series to calculate each term in
 475 (5) and its temperature balance equivalent, with the exception of Q_{-h} , which can be
 476 estimated as the residual between the term on the left and the sum of the first two terms
 477 on the right. We have neglected a term in (5) that is proportional to the horizontal
 478 divergence of the vertically averaged temperature-velocity covariance (see Eq. (A19)
 479 of Moisan and Niiler 1998) because Foltz and McPhaden (2009) found that this term
 480 is insignificant in comparison to the other terms (annual means and monthly standard
 481 deviations are less than 2 W m^{-2}). Horizontal eddy heat advection on timescales less
 482 than one week is also not included in (5) because it cannot be calculated reliably using
 483 observations. This term may be important on the equator, where there are strong SST
 484 gradients and intraseasonal fluctuations of near-surface currents.

485 We estimate the shortwave radiation that penetrates through the base of the
 486 mixed layer using an algorithm that depends on the surface chlorophyll-a concentration
 487 (chl-a), following Morel and Antoine (1994) and Sweeney et al. (2005) and using
 488 the 1998–2009 monthly mean seasonal cycle of chl-a from SeaWiFS. Algorithms that
 489 account for chl-a provide a significant improvement over those that rely on broader
 490 water type classifications (Ohlmann 2003). An albedo of 6% (Payne 1972) is applied
 491 to the surface shortwave radiation before calculation of the penetrative component.
 492 The latent and sensible heat fluxes are calculated with version 3 of the Coupled Ocean
 493 Atmosphere Response Experiment (COARE) bulk algorithm (Fairall et al. 2003) using
 494 the ePIRATA air temperature, relative humidity, wind speed, and SST time series. The
 495 ePIRATA mixed layer depth, mixed layer temperature, horizontal mixed layer velocity,

496 and SST gradients are used to calculate heat storage rate and horizontal advection
497 (first and second terms in the equation). Because the Q_{-h} term is difficult to calculate
498 directly, we do not provide direct estimates of this term in our data set.

499 Each term of the mixed layer temperature budget is also provided in the data
500 set for more direct diagnosis of SST variability. The ePIRATA data set contains daily-
501 averaged values of each term in the heat and temperature budget equations at the
502 17 long-term PIRATA mooring locations, as well as daily time series of data used to
503 calculate the budget terms, the depth of the 20°C isotherm, and isothermal layer depth
504 (useful for calculating barrier layer thickness). Error estimates for these terms are also
505 provided (see Appendix for details of their calculation). Figure 9 shows the time period
506 over which ePIRATA data are available at each location.

507 **3 Results**

508 Here we present examples of ePIRATA at selected locations and illustrate the usefulness
509 of the time series for examining the processes responsible for changes in mixed layer
510 heat content and SST. Near-surface temperature from ePIRATA at 12°N, 38°W shows
511 strong seasonal variations (Figure 10a) tied to meridional movement of the ITCZ and
512 associated changes in wind speed and surface solar radiation (e.g. Foltz et al. 2003,
513 Yu et al. 2006). The mixed layer depth and thermocline depth vary in phase (black
514 and white lines in Figure 10a, respectively), becoming shallowest in boreal summer and
515 fall when the ITCZ is farthest north. Interannual variations of SST can be seen, most
516 notably strong warm events in early 2005 and in 2010. Surface salinity also undergoes a
517 strong seasonal cycle at 12°N, 38°W (Figure 10b), decreasing abruptly in boreal fall and
518 winter as low-salinity water from the ITCZ and Amazon River outflow is transported

519 northward (e.g. Coles et al. 2013, Foltz et al. 2015). At 0° , 23°W the mixed layer
 520 and thermocline depths have weaker seasonal cycles compared to 12°N , 38°W (Figure
 521 10a,c). Near-surface salinity also undergoes weaker seasonal variability at 0° , 23°W ,
 522 with lowest values generally during boreal winter and spring (Figure 10d), when SST
 523 and rainfall are highest and vertical mixing and entrainment of saltier thermocline
 524 water are weakest (e.g. Da-Allada et al. 2013).

525 To illustrate the value of ePIRATA for heat budget studies, we show the daily
 526 mixed layer heat storage rate, surface heat flux components, and horizontal mixed layer
 527 heat advection at 0° , 23°W (Figure 11). Changes in heat storage rate show strong
 528 short-timescale variations (Figure 11a) that are likely caused by lateral movements
 529 of the equatorial SST front. Error bars for the daily heat storage rate are generally
 530 less than 100 W m^{-2} , but become much larger when PIRATA data are unavailable
 531 and satellite SST or Argo data are used to fill the gaps (i.e., early 2005, middle of
 532 2009, and late 2014). A full description of the errors is provided in the Appendix. The
 533 amount of shortwave radiation absorbed in the mixed layer (Figure 11b) shows a strong
 534 seasonal cycle. Error bars on this term are often less than 10 W m^{-2} , but increase to
 535 $20\text{--}40 \text{ W m}^{-2}$ when gaps in the PIRATA record are filled with satellite data. There
 536 are strong seasonal and interannual variations of latent heat flux, and error bars are
 537 consistently about 25 W m^{-2} (Figure 11c). Finally, horizontal heat advection at 0° ,
 538 23°W (Figure 11d) shows strong variability on daily to weekly timescales, peaking in
 539 boreal summer and fall, when the cold tongue is present and tropical instability wave
 540 (TIW) activity is strongest. In many years there is a secondary peak of variability in
 541 boreal winter, possibly related to the November–December central equatorial Atlantic
 542 zonal mode (Okumura and Xie 2006). Errors show a similar seasonality, reaching

543 150 W m^{-2} or higher in boreal summer and fall and dropping to about 50 W m^{-2}
 544 during the rest of the year. The large errors in summer, often exceeding the actual
 545 magnitude of horizontal advection, are caused by strong TIW velocities of up to 80
 546 cm s^{-1} , combined with large uncertainties involved with estimating SST gradients with
 547 satellite data. Note that when averaged to monthly means, the errors are reduced by
 548 a factor of $3/\sqrt{3}$, as discussed later in this section. For climatological monthly means
 549 the errors are reduced by an additional factor of 2.8–4.1 because each ePIRATA time
 550 series is 8–17 years long. Therefore, daily advection errors of 150 W m^{-2} are reduced
 551 to about 20 W m^{-2} for climatological monthly mean advection (Figure 12). The heat
 552 budget terms show noticeable seasonal variations (Figure 12) and seasonal modulations
 553 of interannual variability (vertical bars in Figure 12), with the largest variances in heat
 554 storage rate and advection during boreal summer, when the cold tongue is developed,
 555 and strongest interannual variations of shortwave radiation in boreal spring, when the
 556 ITCZ is near the equator.

557 One of the least frequently measured and least well understood components of
 558 the mixed layer heat budget is vertical turbulent mixing across the base of the mixed
 559 layer (Q_{-h}). This term can be estimated at each ePIRATA location as the difference
 560 between the mixed layer heat storage rate and the sum of the net surface heat flux
 561 and horizontal advection. These estimates must be viewed with caution because of
 562 the accumulation of errors from other terms in the heat balance. However, comparison
 563 of heat budget residuals to more direct measurements of the turbulent heat flux has
 564 shown good agreement (e.g., Moum et al. 2013, Hummels et al. 2014), indicating that
 565 the residual can be used with some confidence to estimate vertical turbulent cooling.
 566 Estimates of vertical turbulent cooling based on parameterizations (e.g., Niiler and

567 Kraus 1977, McPhaden 1982, Stevenson and Niiler 1983) are not provided in ePIRATA
 568 because of large uncertainties inherent in their calculations and in choosing the proper
 569 parameters and constants.

570 We first calculate the monthly mean seasonal cycle of each term in the heat budget
 571 from its daily time series and then compute record-length means. Errors are calculated
 572 using standard error propagation and then multiplied by $3/\sqrt{3}$ to account for the ~ 3 -
 573 day decorrelation timescale found for most variables. At all off-equatorial locations,
 574 the record-length mean Q_{-h} is between -60 and -20 W m^{-2} (Figure 13; negative values
 575 indicate a tendency to cool the mixed layer). The smallest cooling from Q_{-h} occurs at
 576 4°N , 23°W , which experiences weaker mean winds and higher surface solar radiation
 577 compared to many other sites because of its location close to the mean latitude of the
 578 ITCZ. Surprisingly, the other three locations in the ITCZ region, defined as area in
 579 which climatological wind speed is less than 5 m s^{-1} for at least three months of the
 580 year (4°N , 8°N , and 12°N along 38°W ; red symbols in Figure 13) have a mean Q_{-h}
 581 that is similar to values at locations outside of the equatorial and ITCZ bands (blue
 582 symbols in Figure 13). On the equator, there is significantly more cooling from Q_{-h}
 583 at 10°W , 23°W , and 35°W , with mean values of -110 to -85 W m^{-2} (green symbols
 584 in Figure 13). In contrast, the mean Q_{-h} at 0° , 0° is comparable to that found at
 585 the off-equatorial sites. This reduction in cooling at 0° , 0° is believed to be caused
 586 by a decrease in vertical current shear (Jouanno et al. 2011, Hummels et al. 2014,
 587 Giordani and Caniaux 2014). It is unclear why Q_{-h} at 35°W is comparable to that at
 588 10°W and 23°W , since Jouanno et al. (2011) found a significant reduction in vertical
 589 turbulent cooling in the western equatorial Atlantic. Despite this difference, overall the
 590 results are consistent with previous studies, which show the strongest vertical turbulent

591 cooling on the equator (e.g. Foltz et al. 2003, Peter et al. 2006, Hummels et al. 2013).
 592 The ePIRATA estimates of Q_{-h} show strong seasonal variations at many locations,
 593 and the largest peak-to-peak amplitude of 150 W m^{-2} occurs at 0° , 10°W (vertical
 594 lines in Figure 13).

595 To explore the possible causes of seasonal variations of Q_{-h} , we first calculate its
 596 seasonal range, $Q_{-h}(\Delta S) = Q_{-h}(S_{max}) - Q_{-h}(S_{min})$, where S_{max} is the three-month
 597 season (DJF, JFM, FMA, etc.) with the largest mean cooling from Q_{-h} (i.e., most
 598 negative value), and S_{min} is the three-month season with the smallest mean cooling
 599 from Q_{-h} . We then calculate the difference in wind speed between these seasons,
 600 $W(\Delta S) = W(S_{max}) - W(S_{min})$, since wind speed is known to affect the rate of ver-
 601 tical turbulent mixing. We also calculate the difference in the standard deviation of
 602 the diurnal cycle of SST, $D(\Delta S) = D(S_{max}) - D(S_{min})$, using 10-minute averages of
 603 temperature at a depth of 1 m from the PIRATA moorings. The standard deviation
 604 is first calculated for each calendar month using all available 10-minute measurements,
 605 after applying a 36-hour high-pass filter. $D(\Delta S)$ is then calculated from the monthly
 606 values. Studies of turbulent mixing on the equator have indicated that the diurnal cy-
 607 cle is important (e.g., Moum et al. 2011), and here we explore whether the same may
 608 be true at off-equatorial locations in the Atlantic. The diurnal cycle of SST is used as
 609 a proxy for diurnal variations of mixed layer depth and current shear, since previous
 610 studies have shown strong relationships between these parameters (e.g., Cronin and
 611 Kessler 2009).

612 Comparison of $Q_{-h}(\Delta S)$ and $W(\Delta S)$ shows that at 15 of 17 locations, winds
 613 are weaker ($W(\Delta S)$ negative) during the season with the strongest Q_{-h} cooling than
 614 during the season with weakest cooling (Figure 14a). For large negative values of

615 $W(\Delta S)$ ($< 1 \text{ m s}^{-1}$), there is a tendency for larger values of $Q_{-h}(\Delta S)$ to be associated
 616 with larger values of $W(\Delta S)$. At most of these locations, the seasonal range of wind
 617 speed is close to $W(\Delta S)$ (not shown), suggesting that stronger seasonal variations of
 618 wind speed may drive stronger seasonal cycles of Q_{-h} . At off-equatorial locations, the
 619 correlation between $Q_{-h}(\Delta S)$ and $W(\Delta S)$ is 0.53 across all locations (winds are weaker
 620 when cooling is stronger), and this correlation is significant at the 90% level. Along the
 621 equator, the relationship between $Q_{-h}(\Delta S)$ and $W(\Delta S)$ is very weak, likely because
 622 of the importance of seasonal variations in current shear driven by the equatorial
 623 undercurrent (Jouanno et al. 2011, Hummels et al. 2014).

624 The tendency for cooling from Q_{-h} to be strongest when wind speed is weakest
 625 may be related to the tendency for a thinner mixed layer and stronger diurnal cycle
 626 when winds are weak (Fairall et al. 1996a). At 11 of 13 off-equatorial locations, the
 627 mixed layer is thinner in the season with the strongest Q_{-h} cooling than in the season
 628 with the weakest Q_{-h} cooling (not shown). We also found that the diurnal cycle of
 629 SST tends to be stronger in the season with strongest Q_{-h} cooling ($D(\Delta S) > 0$ in
 630 Figure 14b). At off-equatorial locations, the correlation between $Q_{-h}(\Delta S)$ and $D(\Delta S)$
 631 is -0.64 (diurnal cycle is stronger when cooling is stronger), significant at the 95% level.
 632 The correlation drops to -0.43 when equatorial sites are included.

633 Previous studies have shown the importance of the diurnal cycle for generating
 634 vertical current shear and vertical turbulent mixing in the equatorial Pacific (Cronin
 635 and Kessler 2009, Moum et al. 2011, Smyth et al. 2013, Pham et al. 2013) and
 636 Atlantic (Wenegrat et al. 2015). Stronger and shallower stratification during daytime
 637 is associated with stronger near-surface currents and vertical shear, which descends
 638 and generates enhanced turbulent mixing as surface solar heating decreases. On the

639 equator, the equatorial undercurrent provides an essential source of vertical current
 640 shear, explaining the large annual mean turbulent cooling on the equator (Figure 13,
 641 Jouanno et al. 2011, Hummels et al. 2014). We hypothesize that even at off-equatorial
 642 locations, there may be enough diurnally-driven current shear below the mixed layer
 643 and mixed layer deepening (i.e., entrainment mixing) to generate significant turbulent
 644 cooling of the mixed layer. Despite weaker winds when the diurnal cycle is most
 645 active, the thinner mixed layer and stronger stratification may lead to stronger near-
 646 surface current shear than during periods without a strong diurnal cycle, thus possibly
 647 explaining the tendency for Q_{-h} to be largest when winds are weakest and the diurnal
 648 cycle is strongest (Figure 14).

649 The importance of the diurnal cycle may also explain why at off-equatorial lo-
 650 cations the annual mean Q_{-h} values are similar, even with annual mean wind speed
 651 varying between 4.5 and 7 m s⁻¹. At locations with stronger mean winds, the mixed
 652 layer tends to be thicker (correlation between annual mean wind speed and mixed layer
 653 depth is 0.4 across all off-equatorial locations) and the diurnal SST standard deviation
 654 tends to be smaller (correlation of -0.8 between annual mean wind speed and diurnal
 655 SST standard deviation). Stronger winds by themselves tend to generate more mixing,
 656 but at the base of the mixed layer this increase may be balanced by a decrease in
 657 mixing because of an increase in mixed layer depth, acting to reduce current shear,
 658 and a decrease in diurnal cycle amplitude and associated entrainment cooling. These
 659 hypotheses will need to be tested using numerical models and direct measurements of
 660 current shear and turbulent mixing.

661 4 Summary

662 A new daily enhanced PIRATA (ePIRATA) data set has been developed that fills
663 temporal gaps and maps subsurface temperature and salinity to depths of 1 m and with
664 5-m vertical spacing between 5 m and 200 m. All original PIRATA data are retained
665 after elimination of questionable data, and detailed error estimates are provided. The
666 resultant continuous daily time series at each of the 17 PIRATA locations are then
667 used to calculate the terms in the mixed layer heat and temperature budgets and their
668 error bars. This data set complements the tropical Atlantic portions of global data
669 sets such as OAFlux, TropFlux, and OSCAR, which use PIRATA measurements only
670 for validation or to correct for biases. In contrast, ePIRATA consists of the highest-
671 quality basin-scale, co-located time series of upper-ocean and near-surface atmospheric
672 measurements, which we anticipate will be valuable for studies of the upper ocean and
673 air-sea heat and moisture exchange. ePIRATA is available from [http://www.aoml.](http://www.aoml.noaa.gov/phod/epirata/)
674 [noaa.gov/phod/epirata/](http://www.aoml.noaa.gov/phod/epirata/) and will be updated in the middle of each year to extend
675 through the end of the previous year.

676 As an example of the application of ePIRATA, the vertical turbulent exchange
677 of heat across the base of the mixed layer was estimated as the difference between the
678 mixed layer heat storage rate and the sum of the net surface heat flux and horizontal
679 advection at each ePIRATA location. On average, vertical mixing acts to reduce the
680 mixed layer heat content at off-equatorial locations and 0° , 0° by $20\text{--}60\text{ W m}^{-2}$. On
681 the equator at 10°W , 23°W , and 35°W , mean rates of heat content reduction are 85--
682 110 W m^{-2} . Significant seasonal variations of vertical turbulent cooling are found at
683 most locations, and the largest peak-to-peak amplitude of 150 W m^{-2} was found at
684 0° , 10°W . Off the equator, the seasonal maximum of turbulent cooling tends to occur

685 when winds are weak and diurnal variability of SST is strong. These results suggest
686 that the interplay between the diurnal cycle, stratification, and current shear may be
687 important for explaining off-equatorial vertical turbulent cooling of the mixed layer.

688 In addition to its value for upper-ocean and climate research and model vali-
689 dation, ePIRATA presents a framework for assessing the value of additional PIRATA
690 sensors for reducing uncertainties in upper-ocean temperature and salinity, mixed layer
691 depth and currents, and mixed layer heat and temperature budget components. It is
692 anticipated that the largest potential to reduce uncertainties in mixed layer depth and
693 currents is through the addition of one or two current meters in the mixed layer at
694 each mooring location and additional salinity sensors in the upper 50–100 m.

695

696 **Acknowledgments**

697 Support was provided by the Ocean Observations and Monitoring Division of NOAA’s
698 Climate Program Office and by base funds to NOAA’s Atlantic Oceanographic and Me-
699 teorological Laboratory. We are grateful to the U.S., French, and Brazilian PIRATA
700 teams and the TAO Project Office for maintaining the array and providing data free
701 to the public. Argo data were obtained from a Global Data Assembly Centre (Argo
702 GDAC, doi: 10.17882/42182). We thank three anonymous reviewers, whose helpful
703 comments improved the quality of the manuscript.

704

705 **Appendix: Data Availability and Error Estimates**

706 In this appendix we briefly summarize the availability of data at each PIRATA location
707 and the agreement between PIRATA measurements and the reconstructed data used
708 to fill gaps. We then describe the methodology used to calculate error bars for each of

the daily ePIRATA parameters described in the main text. These errors are included in the ePIRATA data set along with the corresponding daily time series of each parameter. Also included in the data set are flags indicating the quality of the data that went into the calculation of each parameter. A flag of '0' indicates that some or all of the data that went into the calculation of that parameter came from sources other than PIRATA (for example, a value of '0' is assigned for temperature at a depth of 50 m if a direct measurement from a PIRATA sensor is not available on that day at that depth). A flag of '1' indicates that original PIRATA data were used, and '2' means that original PIRATA data were used, but a bias correction was applied (applicable for shortwave data at several locations between 8°N and 20.5°N).

719

1. PIRATA Data Availability and Quality of Reconstructed Data

Table A1 shows the percentage of days with missing data for each variable at each location. For this calculation, we take into account only the period after the start of the time series for a given variable begins at a given location. For this reason, there are blanks in Table A1 if a parameter has never been measured. For subsurface temperature and salinity, all depth levels are used in the calculation. The availability of PIRATA data varies across locations and variables (Table A1). In general, there are more missing subsurface temperature, salinity, and velocity data than meteorological data. At many locations, more than 25% of the data are missing for at least one variable, and in some cases 40% or more of salinity or velocity is missing. Note that the high percentage of missing longwave radiation data at 20°N, 38°W results from measurements made for only about two months in 2011 and 10 months in 2013, after which the longwave radiation sensor was not re-deployed.

Table A2 shows the agreement between daily mean PIRATA measurements and the data used to fill gaps in the PIRATA meteorological records. The RMS differences and correlations are calculated using days when both the PIRATA measurements and gap-filling data are available. Correlations are generally highest for air temperature and wind speed (0.89–0.99) and lower for relative humidity and radiation (0.60–0.94). The agreement is good for SST, with correlations of at least 0.8, but worse for sea surface salinity (SSS) and 10-m ocean velocity, with correlations generally between 0.4 and 0.8 (Table A3). The near-zero correlation for SSS at 19°S, 34°W is due to a very weak seasonal cycle of SSS, resulting in a very low signal-to-noise ratio for the satellite SSS used to fill gaps.

1. Ocean Temperature and Salinity Errors

Errors in subsurface temperature and salinity result primarily from (1) vertical interpolation between PIRATA depth levels, (2) filling of temporal gaps in PIRATA records with Argo optimum interpolation, and (3) PIRATA instrumental uncertainties. Errors from (1) and (3) are only applicable when PIRATA data at more than one depth are available on a given day (otherwise Argo optimum interpolation is used and the mooring data are not), and (2) is only relevant when PIRATA data are available at zero or one depth. For (1), all Argo profiles within $\pm 2^\circ$ of latitude and $\pm 3^\circ$ of longitude from a given mooring, and within ± 30 days of a given mooring day (regardless of the year in which the Argo data reside) are obtained. These profiles are then used to calculate the RMS difference between the interpolated temperature or salinity at each missing level, based on the regression method described in section 2.2.1, and the actual Argo temperature or salinity at that level. For PIRATA days on which temperature

757 or salinity at a depth of 1 m has been filled with satellite SST or SSS, respectively, the
 758 uncertainty at that level is instead estimated as the RMS difference between PIRATA
 759 and satellite SST or SSS for that climatological day. The result is an uncertainty esti-
 760 mate, consisting of one of the aforementioned RMS differences, for each day on which
 761 PIRATA measurements at a minimum of two depth levels are available.

762 To calculate uncertainties for case (2), in which PIRATA measurements are avail-
 763 able at less than two depths on a given day, we perform optimum interpolation at each
 764 Argo profile location within $\pm 10^\circ$ of latitude and $\pm 15^\circ$ of longitude of the mooring,
 765 using all other Argo profiles that are within $\pm 10^\circ$ of latitude and $\pm 15^\circ$ of longitude
 766 and ± 3 months of the profile location and following the methodology used for the
 767 Argo optimum interpolation at the PIRATA locations described in section 2.2.1. The
 768 interpolation is performed at each ePIRATA depth level separately. At each depth, the
 769 RMS difference between the optimally interpolated value and the actual Argo value
 770 is calculated and the monthly climatology of the RMS difference is fit to an annual
 771 harmonic. For a given ePIRATA day and depth, the uncertainty in temperature or
 772 salinity is obtained from the corresponding monthly annual cycle of RMS difference.

773 When PIRATA measurements are available at more than one depth on a given
 774 day, instrumental uncertainties of $\pm 0.003^\circ\text{C}$ and ± 0.02 psu are used for temperature
 775 and salinity, respectively (www.pmel.noaa.gov/tao/proj_over/sensors.shtml), at
 776 the ePIRATA depths corresponding to those measurements. The temperature error at
 777 each depth and on each day (ϵ_T) is calculated from either (1), (2), or (3), and simi-
 778 larly for the salinity error (ϵ_S). When vertical interpolation is used between PIRATA
 779 temperature values, errors are typically $0\text{--}0.5^\circ\text{C}$ at off-equatorial locations, increasing
 780 to $0\text{--}1^\circ\text{C}$ in the eastern equatorial Atlantic. Temperature errors are as high as 2°C

on days when all PIRATA data are missing. Salinity errors are 0–0.15 when vertical interpolation is used, and up to 0.3 when all PIRATA data are missing.

2. Mixed Layer Depth, Velocity, and SST Gradient Errors

We use ePIRATA temperature, salinity, ϵ_T , and ϵ_S to calculate errors in mixed layer depth (MLD). First, for a given day, a random value of the temperature error at each depth is obtained using a normal distribution with a standard deviation set to ϵ_T , and similarly for the salinity error. These random temperature and salinity errors are then added to the ePIRATA temperature and salinity profiles, respectively, for that day. If there is static instability in the resultant density profile, the random error generation is repeated until there is stability or the number of iterations reaches 50, whichever occurs first. The MLD is then calculated from the resultant temperature and salinity profiles. All of the above steps are performed 10 times, giving 10 different MLD values for a given PIRATA day. The standard deviation of these values is then used as the uncertainty estimate for MLD. Typical errors for daily-averaged MLD are 3–10 m, with smallest values along the equator, where mean MLDs are smallest. Relative errors (record-length mean daily error divided by record-length mean MLD) are about 10–25%. The procedure for estimating MLD errors is repeated to calculate errors for isothermal layer depth, depth of the 20°C isotherm, and vertically averaged temperature in the mixed layer.

To calculate errors in the mixed layer velocity estimates, we consider three main sources of uncertainty: (1) use of the drifter-altimetry product to fill gaps in the PIRATA records, (2) converting from 10 m velocity to velocity averaged in the mixed layer, and (3) PIRATA instrumental uncertainty, when direct measurements from cur-

805 rent meters are available. At locations with some PIRATA velocity measurements (Ta-
 806 ble 1), the daily RMS difference between the PIRATA values and the drifter-altimetry
 807 values (ϵV_{fill}) are used for (1). At locations with no direct measurements, we use the
 808 errors from nearby locations with measurements: 4°N , 23°W errors are used at 4°N ,
 809 38°W and 8°N , 38°W ; 15°N , 38°W errors are used at 12°N , 38°W ; 0° , 23°W errors
 810 are used at all equatorial locations; and 10°S , 10°W errors are used at all locations
 811 in the South Atlantic. For errors associated with converting 10 m to mixed layer ve-
 812 locity (2), we use the RMS difference between the mixed layer velocity from monthly
 813 ORAS4 data (1958–2014) and mixed layer velocity predicted by the multiple linear re-
 814 gression described in section 2.2.2 (ϵV_{dz}). A constant value of $\pm 5 \text{ cm s}^{-1}$ is used for all
 815 instrumental errors (ϵV_{instr}) (www.pmel.noaa.gov/tao/proj_over/sensors.shtml).
 816 The total uncertainty in mixed layer velocity (zonal or meridional) at a given location
 817 for a given ePIRATA day is $\epsilon_V = \sqrt{\epsilon V_{fill}^2 + \epsilon V_{dz}^2 + \epsilon V_{instr}^2}$ for days with no PIRATA
 818 data at locations with some PIRATA data on other days (ϵV_{instr} is included in this
 819 case because the PIRATA seasonal cycle is added to anomalies of drifter/altimetry or
 820 OSCAR velocity), $\epsilon_V = \sqrt{\epsilon V_{fill}^2 + \epsilon V_{dz}^2}$ for locations with no PIRATA velocity data,
 821 and $\epsilon_V = \sqrt{\epsilon V_{dz}^2 + \epsilon V_{instr}^2}$ for days with PIRATA data. Daily velocity errors range from
 822 5–30 cm s^{-1} within 4° of the equator and decrease to 5–10 cm s^{-1} poleward of 4°N .

823 To calculate errors in horizontal gradients of SST ϵ_{SST} , first the RMS difference
 824 between daily satellite SST and daily PIRATA temperature at a depth of 1 m is calcu-
 825 lated for each calendar month using data from all years. Errors in the zonal gradient
 826 of SST are calculated as $\epsilon_{dx} = \sqrt{2\epsilon_{SST}^2}/\Delta x$. Here Δx is the one-degree distance (in
 827 meters) centered on each PIRATA location. Errors in the meridional gradients of SST
 828 are calculated similarly. Errors in horizontal heat advection are calculated from the

errors in MLD, velocity, and SST gradients using standard error propagation and assuming that the errors in each term are uncorrelated.

3. Atmospheric Data Errors

There are four main sources of error in ePIRATA surface shortwave radiation (SWR).

(1) Uncertainties associated with estimating SWR from satellite OLR are calculated at each location as the RMS difference between daily PIRATA SWR and OLR-based SWR within a given calendar month, using data from all years (ϵSWR_{OLR}). (2) The uncertainty in using the clear-sky method to correct PIRATA SWR for biases caused by dust buildup is calculated as the standard deviation of the daily clear-sky bias at 14°S, 32°W, where the dust-induced bias is very close to zero (ϵSWR_{CS}). This gives a single number (7 W m⁻²) that is used across all locations and for all days. (3) Errors due to short-duration (less than about one month) dust deposition events that are not fully accounted for in the clear-sky correction technique are estimated to be 20% of the SWR correction applied on a given day (ϵSWR_{ST}). (4) Instrumental error of $\pm 2\%$ is used for the PIRATA solar radiometers (ϵSWR_{instr}). On days for which PIRATA SWR is not available and OLR-based SWR is used instead, the total error is calculated as $\epsilon_{SWR} = \sqrt{\epsilon SWR_{instr}^2 + \epsilon SWR_{OLR}^2}$. Note that instrumental errors are included here because the OLR-based SWR anomalies are added to the mean seasonal cycle of mooring SWR, and similarly for other atmospheric time series described later in this section. On days with direct PIRATA measurements for which a dust correction was applied, the error is $\epsilon_{SWR} = \sqrt{\epsilon SWR_{instr}^2 + \epsilon SWR_{CS}^2 + \epsilon SWR_{ST}^2}$. On days with PIRATA measurements and no dust correction, the error is $\epsilon_{SWR} = \epsilon SWR_{instr}$.

At locations where long time series of PIRATA downward longwave radiation

(dLWR) are available, the error is estimated as the RMS difference between daily
 PIRATA dLWR and ERA-interim dLWR for each calendar month, across all years
 (ϵLWR_{fill}). Otherwise, we use the RMS difference from 0° , 23°W for the other equato-
 rial locations; 10°S , 10°W for 6°S , 10°W ; 15°N , 38°W for all other locations along 38°W
 and 23°W ; and 19°S , 34°W for 8°S , 30°W and 14°S , 32°W . Instrumental error of 1% is
 applied only when PIRATA data are available ($\epsilon LWR_{instr.}$). The total error in dLWR
 is calculated as $\epsilon_{dLWR} = \sqrt{\epsilon LWR_{instr.}^2 + \epsilon LWR_{fill}^2}$ on days in which ERA-interim val-
 ues are used and $\epsilon_{dLWR} = \epsilon LWR_{instr.}$ on days in which direct PIRATA measurements
 are available. The total error in net LWR is given as $\epsilon_{LWR} = \sqrt{\epsilon_{dLWR}^2 + \epsilon_{uLWR}^2}$, where
 ϵ_{uLWR} is the error in emitted LWR calculated from the SST error and using standard
 error propagation.

For air temperature, relative humidity, and winds, errors include (1) the RMS
 difference between daily PIRATA and ERA-interim values for a given calendar month,
 based on days when PIRATA data is available at a given location and (2) instrumental
 errors of 0.2°C for air temperature, 2.7% for relative humidity, and 0.3 m s^{-1} for wind
 velocity and speed. On days with missing PIRATA data, the errors are calculated as
 square-root of the sum of the squares of the RMS error and the instrumental error,
 and on days with PIRATA measurements, the error is equal to the instrumental error.

Uncertainties for the heat and temperature budget terms are calculated using
 standard error propagation and assuming that the different sources of error for a given
 term are uncorrelated in time. Error estimates for latent and sensible heat fluxes take
 into account the errors in air temperature, relative humidity, wind speed, and SST
 described earlier in the Appendix, as well as uncertainty associated with the use of a
 bulk formula (12% of the daily latent or sensible heat flux value; Fairall et al. 1996b).

877 Typical errors for daily latent, sensible, longwave, and absorbed shortwave heat fluxes
878 are 15–30, 2–7, 5–10, and 5–20 W m^{-2} , respectively. Relative errors (record-length
879 mean daily error divided by mean value) are 10–30% for latent and longwave, 30–
880 100% for sensible, and 5–10% for absorbed shortwave. Daily errors for horizontal heat
881 advection are normally 30–80 W m^{-2} , with maximum values where mixed layer currents
882 are strongest (along the equator and at 4°N). Because of weak annual mean advection
883 and significant short-timescale fluctuations at most locations, relative errors can reach
884 as high as 50 times the record-length mean, especially within 4° of the equator.

References

- Balmaseda, M. A., K. Mogensen, and A. T. Weaver, 2013: Evaluation of the ECMWF ocean reanalysis system ORAS4. *Quart. J. Royal Met. Soc.*, **139**, 1132–1161, doi:10.1002/qj.2063.
- Bombardi, R. J., L. M. V. Carvalho, C. Jones, and M. S. Reboita, 2014: Precipitation over eastern South America and the South Atlantic Sea surface temperature during neutral ENSO periods, *Clim. Dyn.*, **42**, 1553–1568, doi:10.1007/s00382-013-1832-7.
- Bonjean, F., and G. S. E. Lagerloef, 2002: Diagnostic model and analysis of the surface currents in the tropical Pacific Ocean. *J. Phys. Oceanogr.*, **32**, 2938–2954.
- Bourlès, B., and Coauthors, 2008: The PIRATA program: History, accomplishments, and future directions. *Bull. Am. Meteorol. Soc.*, **89**, 1111–1125, doi:10.1175/2008BAMS2462.1.
- Breugem, W.-P., P. Chang, C. J. Jang, J. Mignot, and W. Hazeleger, 2008: Barrier layers and tropical Atlantic SST biases in coupled GCMs. *Tellus A*, **60**, 885–897.
- Carton, J. A., and B. H. Huang, 1994: Warm events in the tropical Atlantic. *J. Phys. Oceanogr.*, **24**, 888–903.
- Chiang, J. C. H., Y. Kushnir, and A. Giannini, 2002, Deconstructing Atlantic intertropical convergence zone variability: Influence of the local cross-equatorial sea surface temperature gradient and remote forcing from the eastern equatorial Pacific. *J. Geophys. Res.*, **107**, 4004, doi:10.1029/2000JD000307.
- Chiang, J. C. H. and D. J. Vimont, 2004: Analogous Pacific and Atlantic meridional modes of tropical atmosphere-ocean variability. *J. Climate*, **17**, 4143–4158, doi:10.1175/JCLI4953.1.

909 Coles, V. J., M. T. Brooks, J. Hopkins, M. R. Stukel, P. L. Yager, and R. R. Hood,
910 2013: The pathways and properties of the Amazon River Plume in the tropical
911 North Atlantic Ocean. *J. Geophys. Res.*, **118**, 6894–6913, doi:10.1002/2013JC008981.

912 Cronin, M. F., and W. S. Kessler, 2009: Near-surface shear flow in the tropical Pacific
913 cold tongue front. *J. Phys. Oceanogr.*, **39**, 1200–1215, doi:10.1175/2008JPO4064.1.

914 Da-Allada, C. Y., G. Alory, Y. du Penhoat, E. Kestenare, F. Durand, and N. M.
915 Houkonnou, 2013: Seasonal mixed-layer salinity balance in the tropical At-
916 lantic Ocean: Mean state and seasonal cycle. *J. Geophys. Res.*, **118**, 332–345,
917 doi:10.1029/2012JC008357.

918 de Boyer Montégut, C., G. Madec, A. S. Fischer, A. Lazar, and D. Iudicone, 2004:
919 Mixed layer depth over the global ocean: An examination of profile data and a
920 profile-based climatology, *J. Geophys. Res.*, **109**, C12003, doi:10.1029/2004JC002378.

921 Dee, D. P., and coauthors, 2011: The ERA-Interim reanalysis: configuration and per-
922 formance of the data assimilation system. *Q.J.R. Meteorol. Soc.*, **137**, 553–597,
923 doi: 10.1002/qj.828.

924 Ebuchi, N., H. C. Graber, and M. J. Caruso, 2002: Evaluation of wind vectors observed
925 by QuikSCAT/SeaWinds using ocean buoy data. *J. Atmos. Ocean. Tech.*, **19**,
926 2049–2062.

927 Fairall, C. W., E. F. Bradley, J. S. Godfrey, G. A. Wick, J. B. Edson, and G. S. Youn,
928 1996a: Cool-skin and warm-layer effects on sea surface temperature. *J. Geophys.*
929 *Res.*, **101**, 1295–1308.

930 Fairall, C. W., E. F. Bradley, D. P. Rogers, J. B. Edson, and G. S. Young, 1996b: Bulk
931 parameterization of air-sea fluxes for Tropical Ocean-Global Atmosphere Coupled
932 Ocean-Atmosphere Response Experiment. *J. Geophys. Res.*, **101**, 3747–3764.

933 Fairall, C. W., E. F. Bradley, J. E. Hare, A. A. Grachev, and J. B. Edson, 2003:
 934 Bulk parameterization of air-sea fluxes: Updates and verification for the COARE
 935 algorithm. *J. Climate*, **16**, 571–591.

936 Foltz, G. R., S. A. Grodsky, J. A. Carton, and M. J. McPhaden, 2003: Seasonal mixed
 937 layer heat budget of the tropical Atlantic Ocean. *J. Geophys. Res. Oceans*, **108**,
 938 3146, doi:10.1029/2002JC001584.

939 Foltz, G. R., and M. J. McPhaden, 2009: Impact of barrier layer thickness on SST
 940 in the central tropical North Atlantic. *J. Climate*, **22**, 285–299, doi:10.1175/
 941 2008JCLI2308.1.

942 Foltz, G. R., M. J. McPhaden, and R. Lumpkin, 2012: A strong Atlantic Meridional
 943 Mode event in 2009: The role of mixed layer dynamics. *J. Climate*, **25**, 363–380,
 944 doi: 10.1175/JCLI-D-11-00150.1.

945 Foltz, G. R., C. Schmid, and R. Lumpkin, 2013a: Seasonal cycle of the mixed layer
 946 heat budget in the northeastern tropical Atlantic Ocean. *J. Climate*, **26**, 8169–
 947 8188, doi:10.1175/JCLI-D-13-00037.1.

948 Foltz, G. R., A. T. Evan, H. P. Freitag, S. Brown, and M. J. McPhaden, 2013b: Dust
 949 accumulation biases in PIRATA shortwave radiation records. *J. Atmos. Ocean.
 950 Tech.*, **30**, 1414–1432, doi:10.1175/JTECH-D-12-00169.1.

951 Foltz, G. R., C. Schmid, and R. Lumpkin, 2015: Transport of surface freshwater from
 952 the equatorial to the subtropical North Atlantic Ocean. *J. Phys. Oceanogr.*, **45**,
 953 1086–1102, doi:10.1175/JPO-D-14-0189.1.

954 Freitag, H. P., M. E. McCarty, C. Nosse, R. Lukas, M. J. McPhaden, and M. F.
 955 Cronin, 1999: COARE Seacat data: Calibrations and quality control procedures.
 956 *NOAA Tech. Memo. ERL PMEL-115*, 89 pp.

957 Gentemann, C. L., F. J. Wentz, C. A. Mears, and D. K. Smith, 2004: In situ validation
958 of Tropical Rainfall Measuring Mission microwave sea surface temperatures. *J.*
959 *Geophys. Res.*, **109**, C04021, doi:10.1029/2003JC002092.

960 Giarolla, E., P. Nobre, M. Malagutti, and L. P. Pezzi, 2005: The Atlantic Equatorial
961 Undercurrent: PIRATA observations and simulations with GFDL Modular Ocean
962 Model at CPTEC. *Geophys. Res. Lett.*, **32**, L10617, doi:10.1029/2004GL022206.

963 Giordani, H., and G. Caniaux, 2014: Lagrangian sources of frontogenesis in the equa-
964 torial Atlantic front. *Clim. Dyn.*, **43**, 3147–3162, doi:10.1007/s00382-014-2293-3.

965 Grodsky, S. A., J. A. Carton, C. Provost, J. Servain, J. A. Lorenzzetti, and M.
966 J. McPhaden, 2005: Tropical instability waves at 0°N, 23°W in the Atlantic: A
967 case study using Pilot Research Moored Array in the Tropical Atlantic (PIRATA)
968 mooring data. *J. Geophys. Res.*, **110**, C08010, doi:10.1029/2005JC002941.

969 Ham, Y.-G., J.-S. Kug, J.-Y. Park, and F.-F. Jin, 2013: Sea surface temperature in
970 the north tropical Atlantic as a trigger for El Niño/Southern Oscillation events.
971 *Nat. Geosci.*, **6**, 112–116, doi:10.1038/ngeo1686.

972 Han, W. Q., and Coauthors, 2008: Dynamics of intraseasonal sea level and thermocline
973 variability in the equatorial Atlantic during 2002–03. *J. Phys. Oceanogr.*, **38**,
974 945–967, doi:10.1175/2008JPO3854.1.

975 Hummels, R., M. Dengler, and B. Bourlès, 2013: Seasonal and regional variability of
976 upper ocean diapycnal heat flux in the Atlantic cold tongue. *Prog. Oceanogr.*,
977 **111**, 52–74, doi:10.1016/j.pocean.2012.11.001.

978 Hummels, R., M. Dengler, P. Brandt, and M. Schlundt, 2014: Diapycnal heat flux
979 and mixed layer heat budget within the Atlantic Cold Tongue. *Clim. Dyn.*, **43**,
980 3179–3199, doi:10.1007/s00382-014-2339-6.

981 Jackett, D. R., and T. J. McDougall, 1995: Minimal adjustment of hydrographic
982 profiles to achieve static stability. *J. Atmos. Ocean. Tech.*, **12**, 381–389.

983 Jouanno, J., F. Marin, Y. du Penhoat, J. Sheinbaum, and J.M. Molines, 2011: Seasonal
984 heat balance in the upper 100 m of the equatorial Atlantic Ocean. *J. Geophys.*
985 *Res.*, **116**, C09003, doi:10.1029/2010JC006912.

986 Kawai, Y., H. Kawamura, S. Takahashi, K. Hosoda, H. Murakami, K. Misako, and L.
987 Guan, 2006: Satellite-based high-resolution global optimum interpolation sea sur-
988 face temperature data. *J. Geophys. Res.*, **111**, C06016, doi:10.1029/2005JC003313.

989 Kossin, J. P., and D. J. Vimont, 2007: A More General Framework for Understanding
990 Atlantic Hurricane Variability and Trends. *Bull. Amer. Meteor. Soc.*, **88**, 1767–
991 1781, doi:10.1175/BAMS-88-11-1767.

992 Kucharski, F., A. Bracco, J. H. Yoo, and F. Molteni, 2007: Low-frequency variability of
993 the Indian monsoon-ENSO relationship and the tropical Atlantic: The weakening
994 of the 1980s and 1990s. *J. Climate*, **20**, 4255–4266, doi:10.1175/JCLI4254.1.

995 Kumar, B. P., J. Vialard, M. Lengaigne, V. S. N. Murty, and M. J. McPhaden,
996 2012: TropFlux: Air-sea fluxes for the global tropical oceans—Description and
997 evaluation. *Clim. Dyn.*, **38**, 1521–1543, doi:10.1007/s00382-011-1115-0.

998 Lake, B. J., S. M. Noor, H. P. Freitag, and M. J. McPhaden, 2003: Calibration proce-
999 dures and instrumental accuracy estimates of ATLAS air temperature and relative
1000 humidity measurements. *NOAA Tech. Memo. OAR PMEL-123*, NOAA/Pacific
1001 Marine Environmental Laboratory, Seattle, WA, 23 pp.

1002 Lefèvre, N., D. Veeda, M. Araujo, and G. Caniaux, 2016: Variability and trends of
1003 carbon parameters at a time series in the eastern tropical Atlantic. *Tellus B*, **68**,
1004 30305, doi:10.3402/tellusb.v68.30305.

- 1005 Locarnini, R. A., A. V. Mishonov, J. I. Antonov, T. P. Boyer, H. E. Garcia, O. K.
1006 Baranova, M. M. Zweng, C. R. Paver, J. R. Reagan, D. R. Johnson, M. Hamilton,
1007 and D. Seidov, 2013. *World Ocean Atlas 2013, Volume 1: Temperature*. S.
1008 Levitus, Ed., A. Mishonov Technical Ed.; NOAA Atlas NESDIS 73, 40 pp.
- 1009 Lumpkin, R., and S. Garzoli, 2011: Interannual to decadal changes in the western
1010 South Atlantic’s surface circulation. *J. Geophys. Res.*, **116**, C01014, doi:10.1029/
1011 2010JC006285.
- 1012 McPhaden, M. J., 1982: Variability in the central equatorial Indian Ocean. Part II:
1013 Oceanic heat and turbulent energy balance. *J. Mar. Res.*, **40**, 403–419.
- 1014 Mitchell, T. P., and J. M. Wallace, 1992: The annual cycle in equatorial convection
1015 and sea surface temperature. *J. Climate*, **5**, 1140–1156.
- 1016 Moisan, J. R., and P. P. Niiler, 1998: The seasonal heat budget of the North Pacific:
1017 Net heat flux and heat storage rates (1950–1990). *J. Phys. Oceanogr.*, **28**, 401–
1018 421.
- 1019 Morel, A., and D. Antoine, 1994: Heating rate within the upper ocean in relation to
1020 its biooptical state. *J. Phys. Oceanogr.*, **24**, 1652–1665.
- 1021 Moum, J. N., J. D. Nash, and W. D. Smyth, 2011: Narrowband oscillations in the
1022 upper-equatorial ocean. Part I: Interpretation as shear instabilities. *J. Phys.*
1023 *Oceanogr.*, **41**, 397–410, doi:10.1175/2010JPO4450.1.
- 1024 Moum, J. N., A. Perlin, J. D. Nash, and M. J. McPhaden, 2013: Seasonal sea surface
1025 cooling in the equatorial Pacific cold tongue controlled by ocean mixing. *Nature*,
1026 500, 64–67, doi:10.1038/nature12363.
- 1027 Niiler, P. P., and E. B. Kraus, 1977: One-dimensional models of the upper ocean.
1028 *Modelling and Prediction of the Upper Layers of the Ocean*, E. B. Kraus, Ed.,

1029 Pergamon, 143–172.

1030 Nobre, C., and J. Shukla, 1996: Variation of sea surface temperature, wind stress, and
1031 rainfall over the tropical Atlantic and South America. *J. Climate*, **9**, 2464–2479.

1032 Nobre, P., R. A. De Almeida, M. Malagutti, and E. Giarolla, 2012: Coupled Ocean-
1033 Atmosphere Variations over the South Atlantic Ocean. *J. Climate*, **25**, 6349–
1034 6358, doi:10.1175/JCLI-D-11-00444.1.

1035 Ohlmann, J. C., 2003: Ocean radiant heating in climate models. *J. Climate*, **16**,
1036 1337–1351, doi:10.1175/1520-0442-16.9.1337.

1037 Okumura, Y., and S.-P. Xie, 2004: Interaction of the Atlantic equatorial cold tongue
1038 and the African monsoon. *J. Climate*, **17**, 3589–3602.

1039 Okumura, Y., and S.-P. Xie, 2006: Some overlooked features of tropical Atlantic
1040 climate leading to a new Niño-like phenomenon. *J. Climate*, **19**, 5859–5874,
1041 doi:10.1175/JCLI3928.1.

1042 Parard, G., J. Boutin, Y. Cuyppers, P. Bouruet-Aubertot, G. Caniaux, 2014: On the
1043 physical and biogeochemical processes driving the high frequency variability of
1044 CO₂ fugacity at 6°S, 10°W: Potential role of the internal waves. *J. Geophys.*
1045 *Res.*, **119**, 8357–8374, doi:10.1002/2014JC009965.

1046 Payne, R. E., 1972: Albedo of the sea surface. *J. Atmos. Sci.*, **29**, 959–970.

1047 Peter, A. C., M. Le Henaff, Y. Du Penhoat, C. E. Menkes, F. Marin, J. Vialard, G. Ca-
1048 niaux, and A. Lazar, 2006: A model study of the seasonal mixed layer heat budget
1049 in the equatorial Atlantic. *J. Geophys. Res.*, **111**, C06014, doi:10.1029/2005JC003157.

1050 Pham, H. T., S. Sarkar, and K. B. Winters, 2013: Large-Eddy Simulation of Deep-
1051 Cycle Turbulence in an Equatorial Undercurrent Model. *J. Phys. Oceanogr.*, **43**,
1052 2490–2502, doi:10.1175/JPO-D-13-016.1.

1053 Polo, I., B. Rodriguez-Fonseca, T. Losada, and J. Garcia-Serrano, 2008: Tropical At-
1054 lantic Variability Modes (1979-2002). Part I: Time-Evolving SST Modes Related
1055 to West African Rainfall. *J. Climate*, **21**, 6457–6475, doi:10.1175/2008JCLI2607.1.

1056 Reul, N., Y. Quilfen, B. Chapron, S. Fournier, V. Kudryavtsev, and R. Sabia, 2014:
1057 Multisensor observations of the Amazon-Orinoco river plume interactions with
1058 hurricanes. *J. Geophys. Res.*, **119**, 8271–8295, doi:10.1002/2014JC010107.

1059 Richter, I., and S.-P. Xie, 2008: On the origin of equatorial Atlantic biases in coupled
1060 general circulation models. *Clim. Dyn.*, **31**, 587–598, doi:10.1007/s00382-008-
1061 0364-z.

1062 Rodriguez-Fonseca, B., I. Polo, J. Garcia-Serrano, T. Losada, E. Mohino, C. R. Me-
1063 choso, and F. Kucharski, 2009: Are Atlantic Ninos enhancing Pacific ENSO
1064 events in recent decades? *Geophys. Res. Lett.*, **36**, L20705, doi:10.1029/2009GL040048.

1065 Rouault, M., J. Servain, C. J. C. Reason, B. Boulès, M. J. Rouault, and N. Fauchereau,
1066 2009: Extension of PIRATA in the tropical Southeast Atlantic: an initial one-year
1067 experiment. *African J. Mar. Sci.*, **31**, 63–71, doi:10.2989/AJMS.2009.31.1.5.776.

1068 Rugg, A., G. R. Foltz, and R. C. Perez, 2016: Role of mixed layer dynamics in tropical
1069 North Atlantic interannual sea surface temperature variability. *J. Climate*, **29**,
1070 8083–8101, doi:10.1175/JCLI-D-1500867.1.

1071 Serra, Y. L., and M. J. McPhaden, 2003: Multiple time- and space-scale comparisons
1072 of ATLAS buoy rain gauge measurements with TRMM satellite precipitation
1073 measurements. *J. Appl. Meteorol.*, **42**, 1045–1059.

1074 Servain, J., and Coauthors, 1998: A Pilot Research Moored Array in the Tropical
1075 Atlantic (PIRATA). *Bull. Am. Meteorol. Soc.*, **79**, 2019–2031.

1076 Smyth, W. D., J. N. Moum, L. Li, and S. A. Thorpe, 2013: Diurnal shear instability,

1077 the descent of the surface shear layer, and the deep cycle of equatorial turbulence.
1078 *J. Phys. Oceanogr.*, **43**, 2432–2455, doi:10.1175/JPO-D-13-089.1.

1079 Stevenson, J. W., and P. P. Niiler, 1983: Upper ocean heat budget during the Hawaii-
1080 to-Tahiti Shuttle Experiment. *J. Phys. Oceanogr.*, **13**, 1894–1907.

1081 Sweeney, C., and Coauthors, 2005: Impacts of shortwave penetration depth on large-
1082 scale ocean circulation and heat transport. *J. Phys. Oceanogr.*, **35**, 1103–1119,
1083 doi:10.1175/JPO2740.1.

1084 Wade, M., G. Caniaux, Y. DuPenhoat, M. Dengler, H. Giordani, and R. Hummels,
1085 2011: A one-dimensional modeling study of the diurnal cycle in the equatorial
1086 Atlantic at the PIRATA buoys during the EGEE-3 campaign. *Ocean Dyn.*, **61**,
1087 1–20, doi:10.1007/s10236-010-0337-8.

1088 Wenegrat, J. O., and M. J. McPhaden, 2015: Dynamics of the surface layer diurnal
1089 cycle in the equatorial Atlantic Ocean (0°, 23°W). *J. Geophys. Res.*, **120**, 563–
1090 581, doi:10.1002/2014JC010504.

1091 Woodruff, S., S. Worley, S. Lubker, Z. Ji, E. Freeman, D. Berry, P. Brohan, E. Kent,
1092 D. Reynolds, S. Smith, and C. Wilkinson, 2011: ICOADS Release 2.5: extensions
1093 and enhancements to the surface marine meteorological archive. *Int. J. Climatol.*,
1094 **31**, 951–967, doi:10.1002/joc.2103.

1095 Yoon, J.-H., and N. Zeng, 2010: An Atlantic influence on Amazon rainfall. *Clim.*
1096 *Dyn.*, **34**, 249–264, doi:10.1007/s00382-009-0551-6.

1097 Yu, L. S., X. Z. Jin, and R. A. Weller, 2006: Role of net surface heat flux in seasonal
1098 variations of sea surface temperature in the tropical Atlantic Ocean. *J. Climate*,
1099 **19**, 6153–6169, doi:10.1175/JCLI3970.1.

1100 Yu, L. S., and R. A. Weller, 2007: Objectively analyzed air-sea heat fluxes for the

1101 global ice-free oceans (1981–2005). *Bull. Am. Meteorol. Soc.*, **88**, 527–539,
 1102 doi:10.1175/BAMS-88-4-527.
 1103 Zebiak, S., 1993: Air-sea interaction in the equatorial Atlantic region, *J. Climate*, **6**,
 1104 1567–1586.
 1105 Zweng, M. M, J. R. Reagan, J. I. Antonov, R. A. Locarnini, A. V. Mishonov, T.
 1106 P. Boyer, H. E. Garcia, O. K. Baranova, D. R. Johnson, D. Seidov, and M. M.
 1107 Biddle, 2013: *World Ocean Atlas 2013, Volume 2: Salinity*. S. Levitus, Ed., A.
 1108 Mishonov Technical Ed.; NOAA Atlas NESDIS 74, 39 pp.

1109 **Table 1** PIRATA locations with downward longwave radiation and 10-m ocean velocity
1110 measurements. Locations with longwave radiation also measure barometric pressure.
1111 Second and third columns indicate beginning years for longwave and velocity mea-
1112 surements, respectively. All measurements continue through the present. Numbers in
1113 italics indicate that the data is contaminated by dust.

	LWR	Vel
20°N, 38°W	<i>2011</i>	2007
15°N, 38°W	2006	2005
20.5°N, 23°W		2007
11.5°N, 23°W	<i>2007</i>	2006
4°N, 23°W		2006
0°, 23°W	2006	2005
10°S, 10°W	2006	2005
19°S, 34°W	2010	

1114 **Table A1** Percentage of daily data that is missing at each PIRATA location. Columns
1115 show values for air temperature (AT), relative humidity (RH), wind speed (WS), short-
1116 wave radiation (SWR), longwave radiation (LWR), ocean temperature (Temp), salinity
1117 (Salin), and velocity at a depth of 10 m (Vel).

1118
1119

	AT	RH	WS	SWR	LWR	Temp	Salin	Vel
20°N, 38°W	14	14	20	25	72	26	36	51
15°N, 38°W	4	5	14	3	21	11	31	41
12°N, 38°W	5	8	17	2		12	32	
8°N, 38°W	14	11	30	9		11	44	
4°N, 38°W	12	10	25	16		20	34	
20.5°N, 23°W	1	9	13	1		10	24	50
11.5°N, 23°W	18	19	16	14	17	15	15	36
4°N, 23°W	1	1	6	19		10	29	41
0°, 35°W	10	7	16	10		14	50	
0°, 23°W	6	6	26	9	16	16	26	58
0°, 10°W	29	38	47	27		33	37	
0°, 0°	30	32	41	34		31	41	
6°S, 10°W	1	1	18	7		10	32	
10°S, 10°W	5	5	10	25	13	9	21	46
8°S, 30°W	9	9	9	9		16	23	
14°S, 32°W	6	6	7	10		10	14	
19°S, 34°W	15	15	9	5	1	10	26	

1120

Table A2 Comparisons between daily PIRATA measurements and data used to fill gaps. Shown are the RMS differences and correlations (in parentheses) at each location for air temperature (AT), relative humidity (RH), wind speed (WS), shortwave radiation (SWR), and longwave radiation (LWR). Calculations at each location are based only on time periods when PIRATA and gap-filling data are available.

1126
1127

	AT	RH	WS	SWR	LWR
20°N, 38°W	0.1 (0.99)	2.1 (0.93)	0.5 (0.97)	20.9 (0.92)	
15°N, 38°W	0.2 (0.99)	3.4 (0.81)	0.5 (0.96)	35.7 (0.73)	6.0 (0.93)
12°N, 38°W	0.3 (0.98)	3.2 (0.76)	0.7 (0.95)	37.6 (0.71)	
8°N, 38°W	0.3 (0.91)	3.0 (0.75)	0.6 (0.96)	42.3 (0.72)	
4°N, 38°W	0.3 (0.90)	2.8 (0.81)	0.6 (0.94)	40.0 (0.78)	
20.5°N, 23°W	0.2 (0.99)	2.2 (0.94)	0.5 (0.97)	24.0 (0.88)	
11.5°N, 23°W	0.2 (0.99)	2.2 (0.88)	0.4 (0.98)	26.4 (0.82)	
4°N, 23°W	0.2 (0.95)	2.4 (0.87)	0.6 (0.95)	32.1 (0.79)	
0°, 35°W	0.3 (0.89)	2.5 (0.78)	0.5 (0.96)	34.0 (0.77)	
0°, 23°W	0.3 (0.96)	3.1 (0.60)	0.5 (0.96)	29.2 (0.70)	4.7 (0.94)
0°, 10°W	0.3 (0.99)	2.4 (0.84)	0.5 (0.93)	28.3 (0.68)	
0°, 0°	0.5 (0.96)	2.5 (0.76)	0.5 (0.93)	32.3 (0.70)	
6°S, 10°W	0.3 (0.99)	3.0 (0.73)	0.4 (0.94)	31.0 (0.67)	
10°S, 10°W	0.3 (0.98)	3.5 (0.66)	0.5 (0.93)	31.2 (0.80)	7.1 (0.79)
8°S, 30°W	0.2 (0.98)	2.0 (0.86)	0.4 (0.96)	20.5 (0.89)	
14°S, 32°W	0.1 (0.99)	2.1 (0.85)	0.4 (0.96)	21.1 (0.91)	
19°S, 34°W	0.2 (0.99)	2.6 (0.90)	0.6 (0.96)	26.7 (0.91)	4.6 (0.95)

1128

Table A3 Same as Table A2, except values for SST, sea surface salinity (SSS), and zonal and meridional velocity at a depth of 10 m (U and V, respectively).

	SST	SSS	U	V
20°N, 38°W	0.3 (0.98)	0.1 (0.38)	8.1 (0.72)	8.7 (0.69)
15°N, 38°W	0.3 (0.98)	0.2 (0.55)	7.8 (0.45)	8.1 (0.40)
12°N, 38°W	0.4 (0.96)	0.2 (0.59)		
8°N, 38°W	0.4 (0.92)	0.4 (0.82)		
4°N, 38°W	0.3 (0.80)	0.2 (0.69)		
20.5°N, 23°W	0.3 (0.99)	0.2 (0.56)	8.1 (0.63)	6.5 (0.72)
11.5°N, 23°W	0.4 (0.98)	0.2 (0.76)	12.3 (0.46)	11.3 (0.50)
4°N, 23°W	0.4 (0.87)	0.3 (0.63)	16.4 (0.56)	18.1 (0.53)
0°, 35°W	0.3 (0.88)	0.2 (0.65)		
0°, 23°W	0.4 (0.96)	0.2 (0.78)	25.5 (0.50)	19.4 (0.40)
0°, 10°W	0.4 (0.98)	0.4 (0.81)		
0°, 0°	0.5 (0.96)	0.3 (0.88)		
6°S, 10°W	0.3 (0.99)	0.1 (0.78)		
10°S, 10°W	0.3 (0.98)	0.1 (0.79)	6.6 (0.52)	6.6 (0.48)
8°S, 30°W	0.2 (0.97)	0.1 (0.63)		
14°S, 32°W	0.3 (0.97)	0.2 (0.67)		
19°S, 34°W	0.3 (0.98)	0.1 (0.06)		

Figure Captions

Figure 1 Annual mean satellite microwave SST (contours, °C). Squares show the locations of the “backbone” PIRATA array, first deployed in 1997. Triangles and circles indicate the positions of the Northeast Extension and Southwest Extension moorings, respectively, first deployed in 2005–06. The black circle shows the position of the Southeast Extension mooring, part of PIRATA since 2013 and not used in this study because of its short duration. Colors indicate the percentage of PIRATA data that are missing at each location, calculated using all sensors and starting on the first day of the first deployment at a given location.

Figure 2 (a) Time series of original PIRATA air temperature (purple), original data that were removed after quality-control (black), bias-corrected ERA-interim data that were used to fill gaps in the quality-controlled time series (red), and difference between SST and air temperature (green) at 0°, 35°W. (b) Same as (a) except relative humidity (purple, black, and red) and relative humidity anomaly from the daily climatology (gray).

Figure 3 Correlation between PIRATA shortwave radiation (SWR) and SWR estimated from outgoing longwave radiation (OLR). Values were computed using anomalies from either the daily mean or monthly mean seasonal cycle. No smoothing was applied to the time series before computing anomalies. At each location, gray bars are for daily mean anomalies and red circles are for monthly mean anomalies. See the Appendix for correlations between time series that include the seasonal cycle.

1158

1159 **Figure 4** (a) Daily time series of salinity at a depth of 20 m (purple, red, and black)
1160 and the difference between salinity at 20 m and at 1 m (gray shading) at the 12°N,
1161 38°W PIRATA location. Purple indicates original PIRATA data that have passed
1162 quality-control. Red shows data that were removed during quality-control, and black
1163 represents the final 20 m salinity record with gaps filled. (b) Same as (a) except data
1164 are from the 0°, 0° mooring. (c) Same as (a) except data are from the 10°S, 10°W
1165 mooring and salinity at a depth of 1 m is shown (purple, red, and black). The green
1166 line shows in (c) shows the difference between salinity at a depth of 10 m and at 1 m.

1167

1168 **Figure 5** (a) RMS difference between temperature from Argo profiles near the 4°N,
1169 38°W mooring and temperature estimated using the Argo regression method (red) and
1170 linear interpolation between the two nearest depths (black). For the regression and in-
1171 terpolation methods, Argo profiles were subsampled every 20 m in depth. (b) Same as
1172 (a) except the mean bias between temperature estimated using the regression method
1173 (red) and linear interpolation (black). (c) and (d) Same as (a) and (b) except at the
1174 0°, 10°W mooring location.

1175

1176 **Figure 6** Same as Figure 5 except for salinity. For the regression and interpola-
1177 tion methods, Argo profiles were subsampled at depths of 1, 20, 40, and 120 m.

1178

1179 **Figure 7** (a) Mixed layer depth (MLD, black), amplitude of the seasonal cycle of
1180 MLD (red), and ratio of the seasonal amplitude of MLD to the standard deviation
1181 of high-frequency (period less than 10 days) MLD variability (purple) as a function

1182 of MLD criterion, based on an increase in density from the value at a depth of 1 m.
1183 Values have been averaged over all daily data and all PIRATA locations. (b) Same
1184 as (a) except difference between SST and mixed layer temperature (ΔT , black) and
1185 amplitude of the seasonal cycle of ΔT (red). Squares in (a) and (b) indicate the values
1186 corresponding to a MLD defined using a 0.12 kg m^{-3} criterion.

1187

1188 **Figure 8** (a) Time series of mixed layer depth (gray shading), zonal velocity at a
1189 depth of 10 m (black), and correction to 10-m velocity used to obtain the velocity
1190 vertically averaged in the mixed layer (green shading) at 0° , 35°W . (b) Same as (a)
1191 except at 6°S , 10°W and velocity correction is shaded purple.

1192

1193 **Figure 9** Availability of daily ePIRATA data at each mooring location. Black in-
1194 dicates “backbone” moorings, red shows Southwest Extension, and green Northeast
1195 Extension.

1196

1197 **Figure 10** ePIRATA (a) temperature (shaded), mixed layer depth (black line), and
1198 depth of the 20°C isotherm (white line) at 12°N , 38°W . (b) Same as (a) except shading
1199 is salinity. (c) and (d) Same as (a) and (b) except at 0° , 10°W .

1200

1201 **Figure 11** ePIRATA data at 0° , 23°W : (a) mixed layer heat storage rate (black line),
1202 (b) shortwave radiation absorbed in the mixed layer (red line), (c) latent heat flux (blue
1203 line), and (d) horizontal mixed layer heat advection (green line). In (a)-(d) shading
1204 indicates error estimates, with values on the right axis.

1205

Figure 12 ePIRATA monthly mean climatological heat budget terms at 0° , 23°W : mixed layer heat storage rate (black line), (b) shortwave radiation absorbed in the mixed layer (red line), (c) latent heat flux (blue line), and (d) horizontal mixed layer heat advection (green line). Shading indicates error estimates and vertical error bars show the standard deviation for each calendar month across all years (a measure of interannual variability).

Figure 13 Heat budget residual (heat storage rate minus sum of net surface heat flux and horizontal advection) at each ePIRATA location. Large symbols represent record-length mean, lines show the range of climatological monthly values, and small symbols are the error estimates for the annual mean. Blue indicates locations outside of the ITCZ and equatorial regions, red shows locations in the ITCZ region, and green is for locations on the equator.

Figure 14 Scatter-plots of the seasonal range of Q_{-h} at each ePIRATA location, calculated as the difference between the three-month season (S_{max}) with the largest mean cooling from Q_{-h} (i.e., most negative value) and the three-month season (S_{min}) with the smallest cooling, versus (a) the corresponding wind speed difference, $W(S_{max}) - W(S_{min})$, and (b) the difference in the diurnal amplitude of SST. Dark blue and light blue indicate locations in the Northern and Southern Hemisphere, respectively, and outside of the ITCZ. Red indicates locations within the ITCZ, and green is for locations on the equator. Bars in (a) represent error estimates for each seasonal difference of Q_{-h} . Error bars for wind speed in (a) and SST in (b) are less than 0.1 m s^{-1} and 0.01°C , respectively, and are not shown.

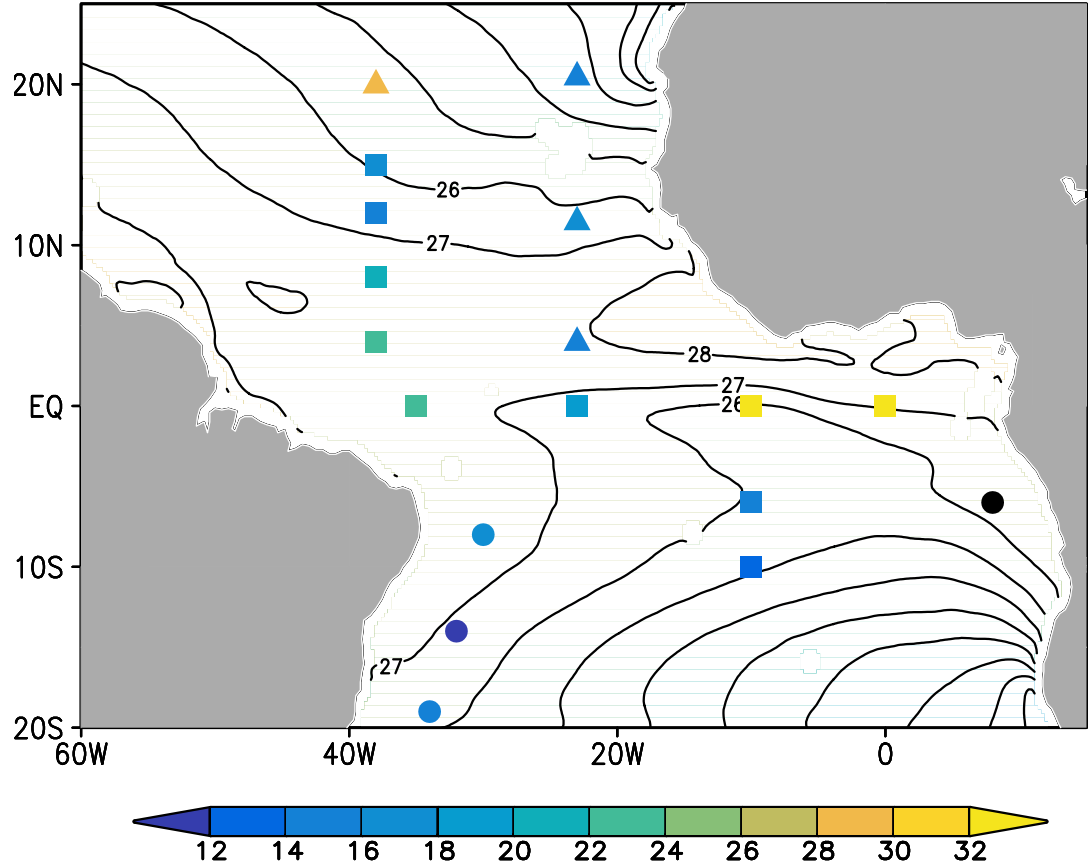


Figure 1 Annual mean satellite microwave SST (contours, °C). Squares show the locations of the “backbone” PIRATA array, first deployed in 1997. Triangles and circles indicate the positions of the Northeast Extension and Southwest Extension moorings, respectively, first deployed in 2005–06. The black circle shows the position of the Southeast Extension mooring, part of PIRATA since 2013 and not used in this study because of its short duration. Colors indicate the percentage of PIRATA data that are missing at each location, calculated using all sensors and starting on the first day of the first deployment at a given location.

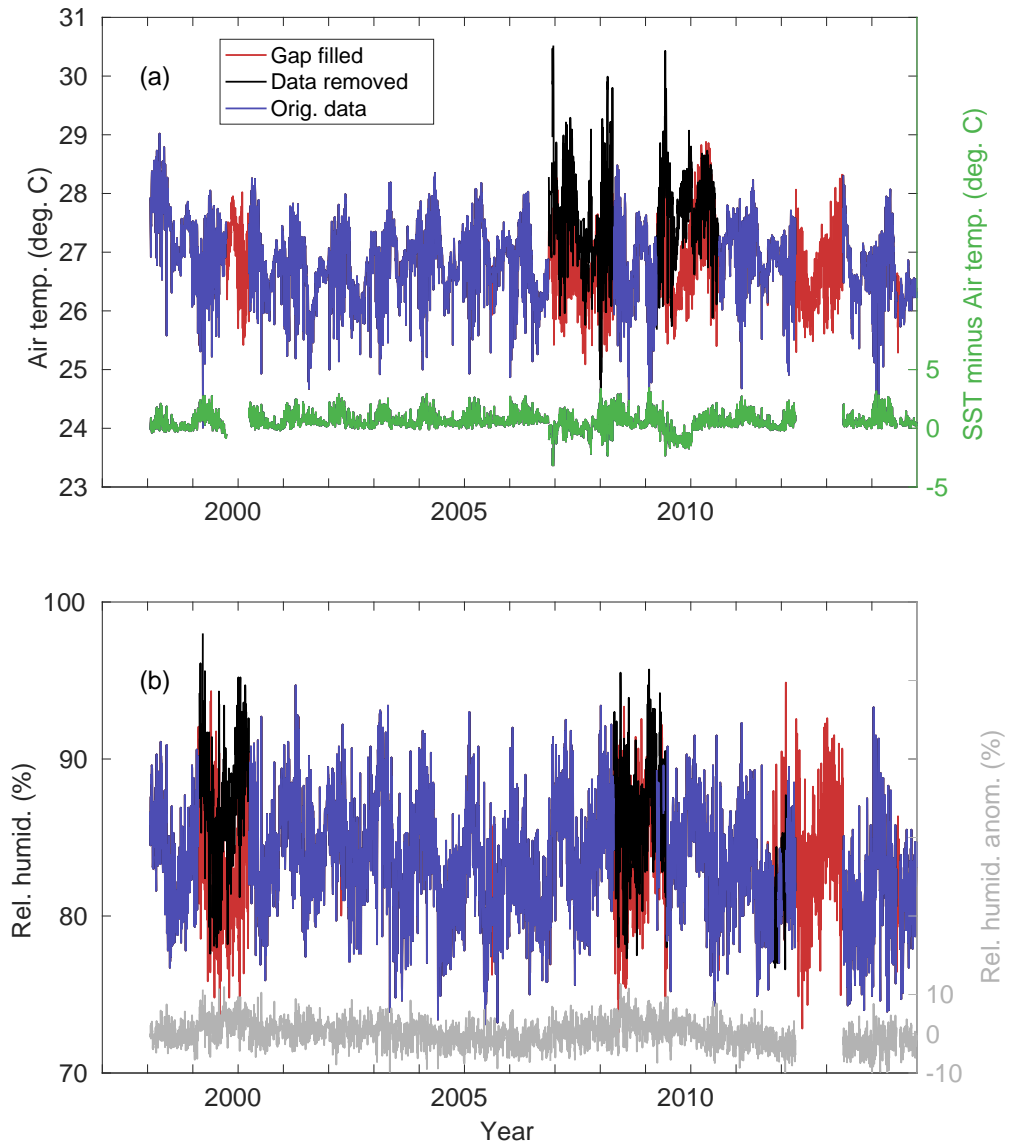


Figure 2 (a) Time series of original PIRATA air temperature (purple), original data that were removed after quality-control (black), bias-corrected ERA-interim data that were used to fill gaps in the quality-controlled time series (red), and difference between SST and air temperature (green) at 0°, 35°W. (b) Same as (a) except relative humidity (purple, black, and red) and relative humidity anomaly from the daily climatology (gray).

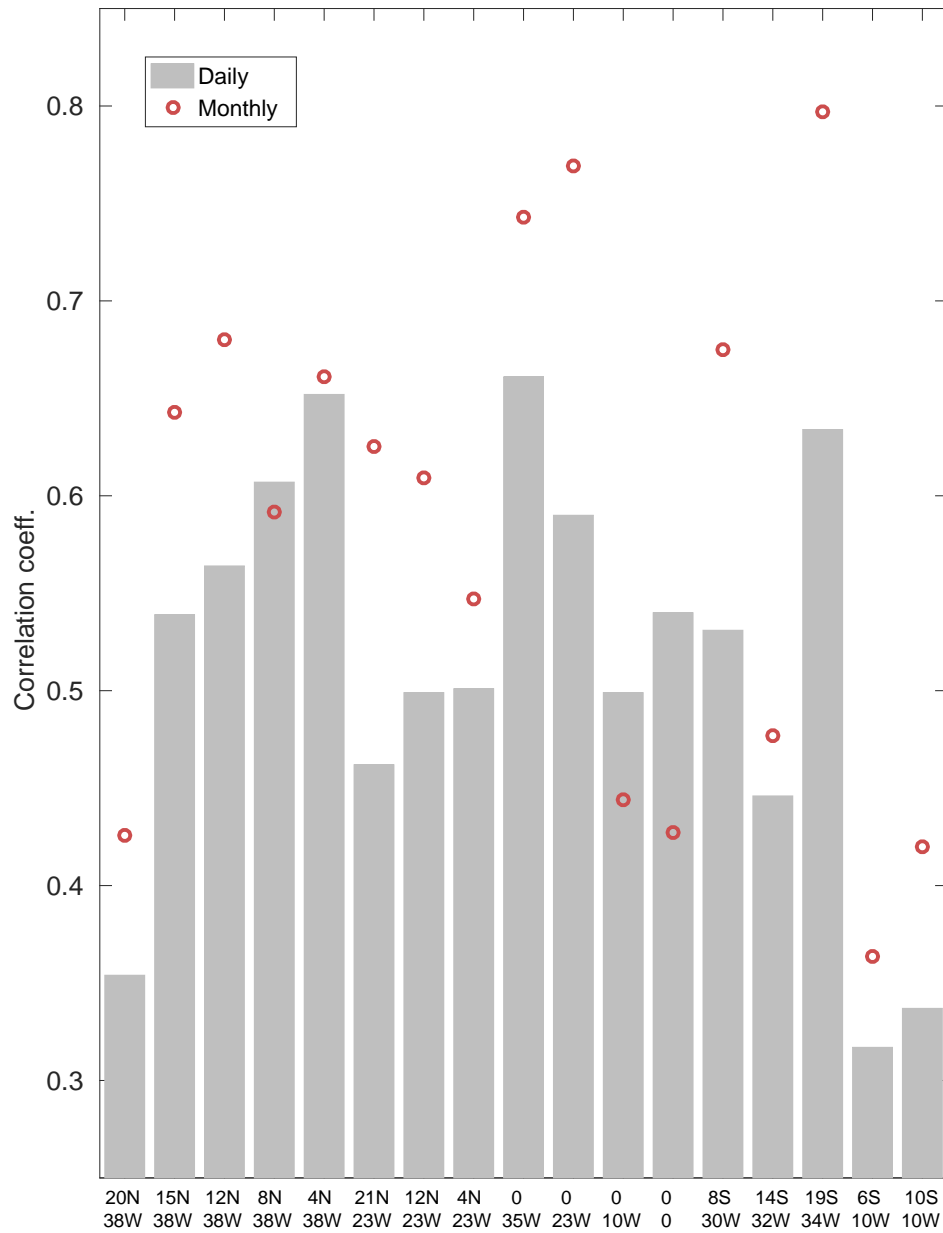


Figure 3 Correlation between PIRATA shortwave radiation (SWR) and SWR estimated from outgoing longwave radiation (OLR). Values were computed using anomalies from either the daily mean or monthly mean seasonal cycle. No smoothing was applied to the time series before computing anomalies. At each location, gray bars are for daily mean anomalies and red circles are for monthly mean anomalies. See the Appendix for correlations between time series that include the seasonal cycle.

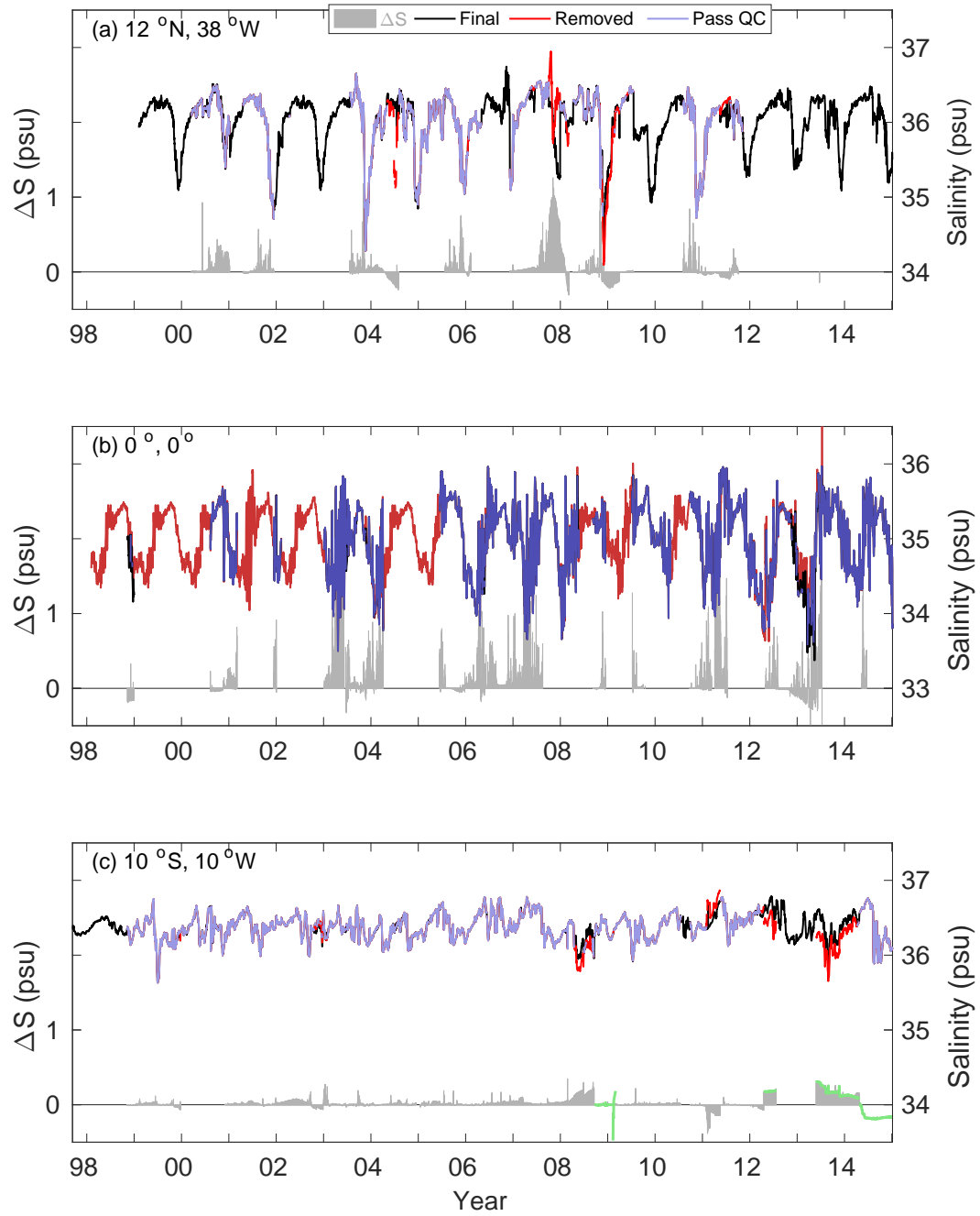


Figure 4 (a) Daily time series of salinity at a depth of 20 m (purple, red, and black) and the difference between salinity at 20 m and at 1 m (gray shading) at the 12°N, 38°W PIRATA location. Purple indicates original PIRATA data that have passed quality-control. Red shows data that were removed during quality-control, and black represents the final 20 m salinity record with gaps filled. (b) Same as (a) except data are from the 0°, 0° mooring. (c) Same as (a) except data are from the 10°S, 10°W mooring and salinity at a depth of 1 m is shown (purple, red, and black). The green line shows in (c) shows the difference between salinity at a depth of 10 m and at 1 m.

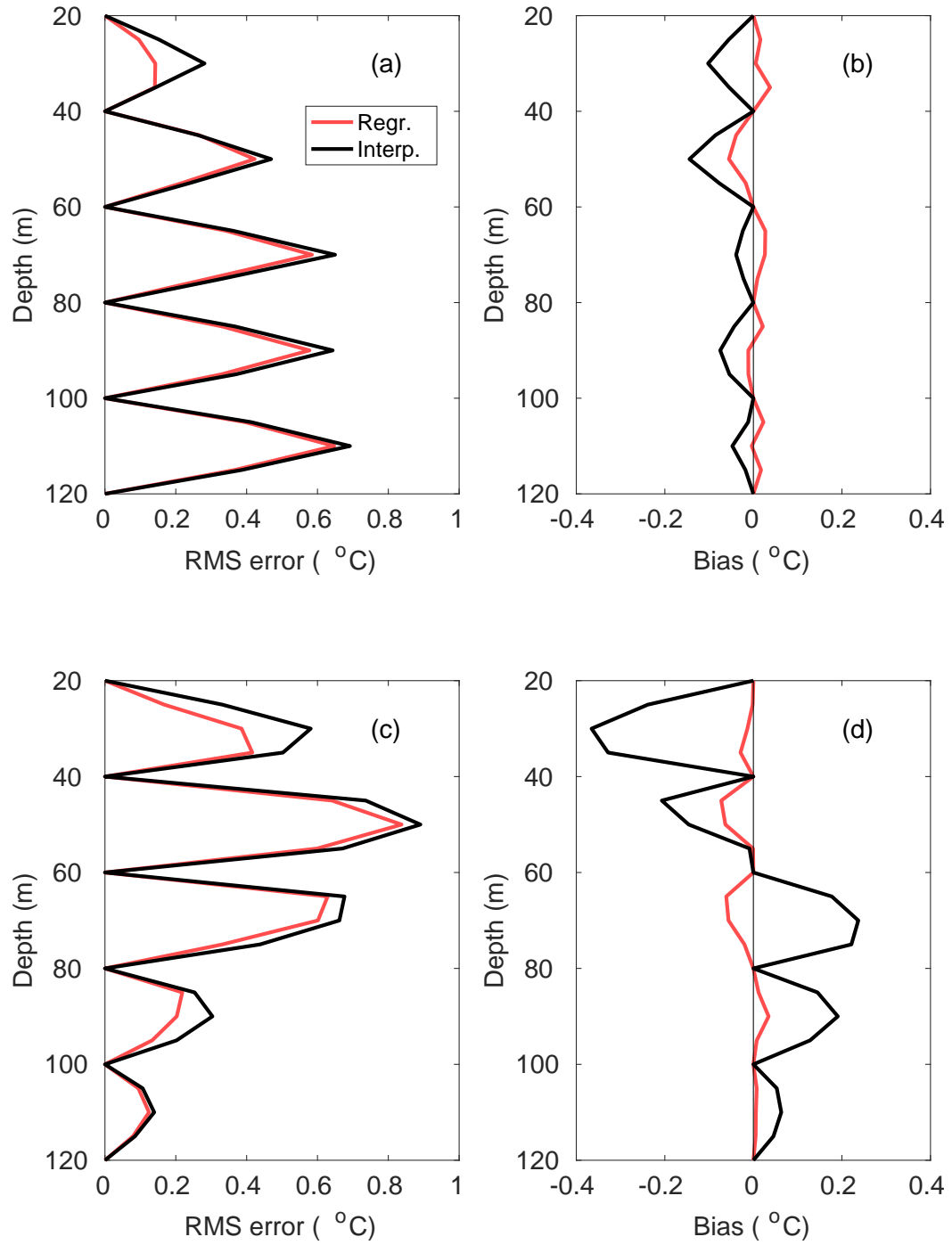


Figure 5 (a) RMS difference between temperature from Argo profiles near the 4°N, 38°W mooring and temperature estimated using the Argo regression method (red) and linear interpolation between the two nearest depths (black). For the regression and interpolation methods, Argo profiles were subsampled every 20 m in depth. (b) Same as (a) except the mean bias between temperature estimated using the regression method (red) and linear interpolation (black). (c) and (d) Same as (a) and (b) except at the 0°, 10°W mooring location.

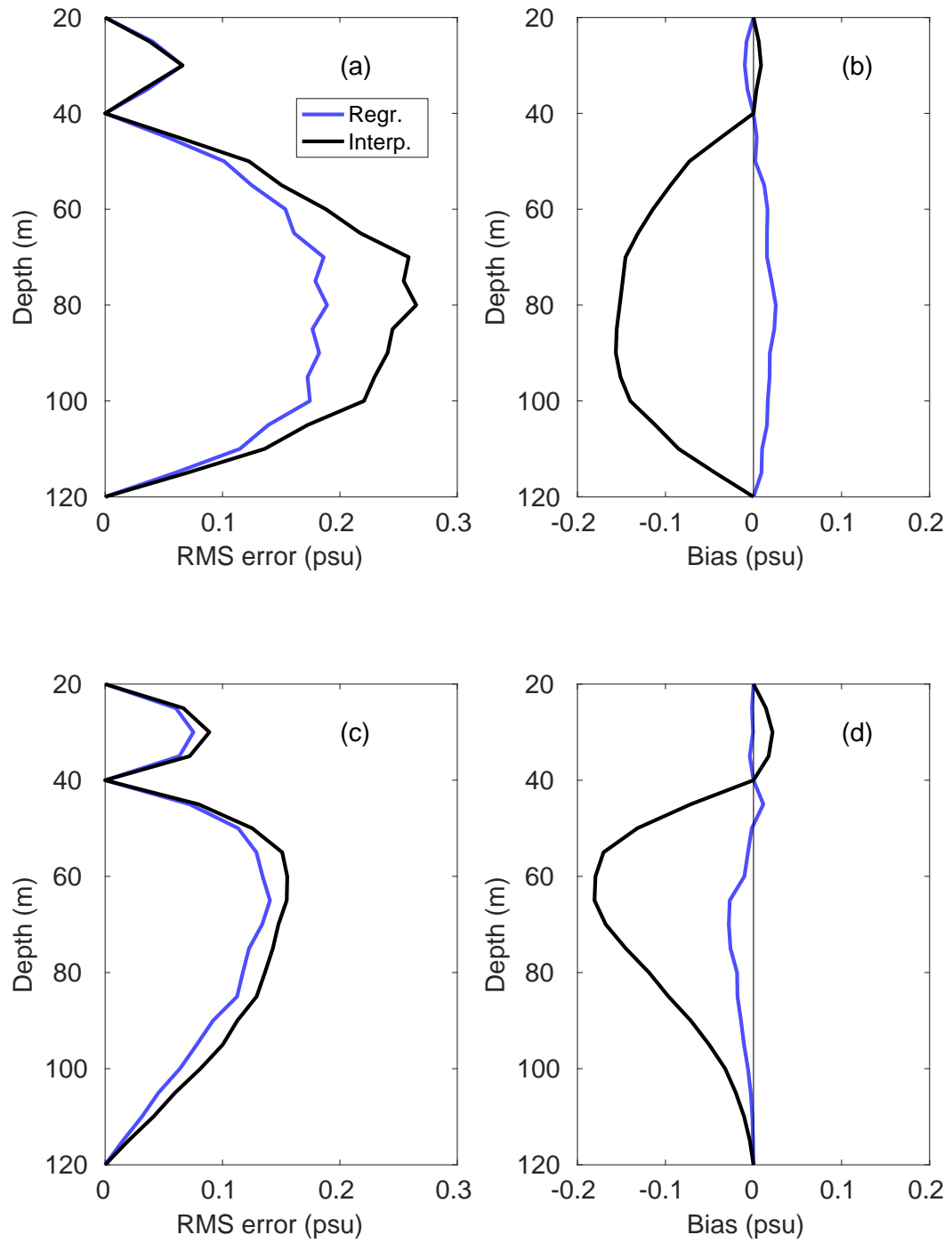


Figure 6 Same as Figure 5 except for salinity. For the regression and interpolation methods, Argo profiles were subsampled at depths of 1, 20, 40, and 120 m.

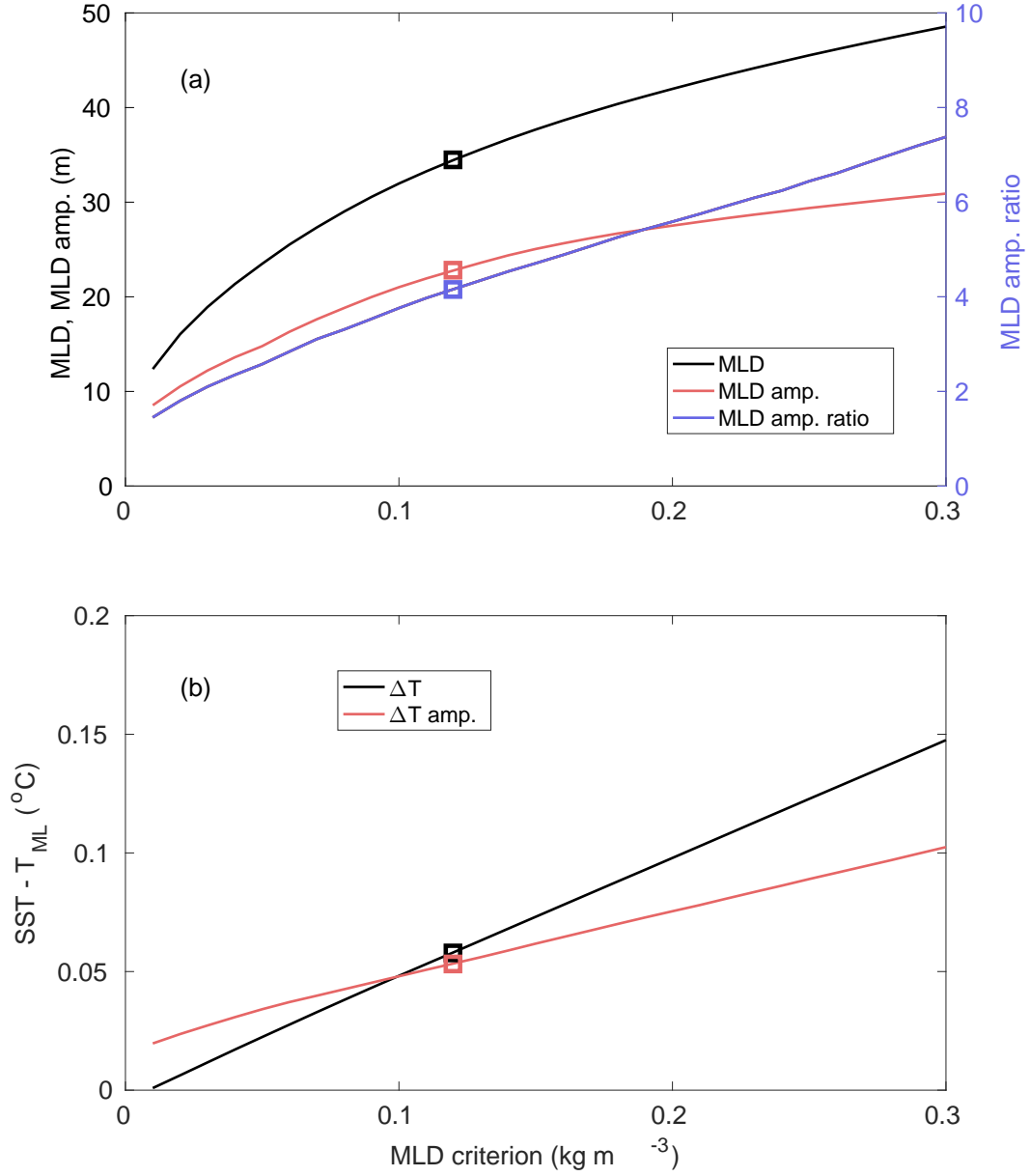


Figure 7 (a) Mixed layer depth (MLD, black), amplitude of the seasonal cycle of MLD (red), and ratio of the seasonal amplitude of MLD to the standard deviation of high-frequency (period less than 10 days) MLD variability (purple) as a function of MLD criterion, based on an increase in density from the value at a depth of 1 m. Values have been averaged over all daily data and all PIRATA locations. (b) Same as (a) except difference between SST and mixed layer temperature (ΔT , black) and amplitude of the seasonal cycle of ΔT (red). Squares in (a) and (b) indicate the values corresponding to a MLD defined using a 0.12 kg m^{-3} criterion.

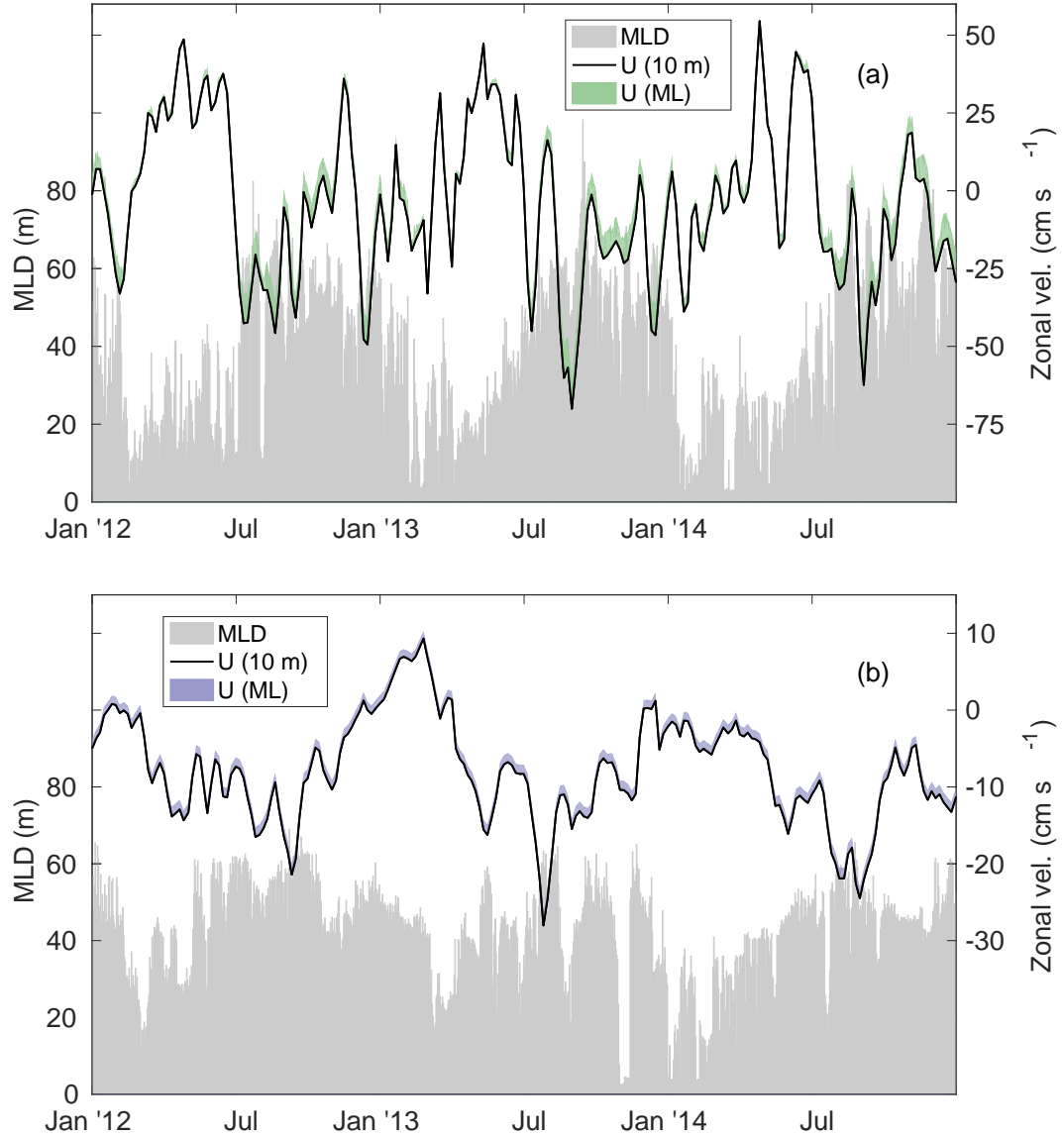


Figure 8 (a) Time series of mixed layer depth (gray shading), zonal velocity at a depth of 10 m (black), and correction to 10-m velocity used to obtain the velocity vertically averaged in the mixed layer (green shading) at 0°, 35°W. (b) Same as (a) except at 6°S, 10°W and velocity correction is shaded purple.

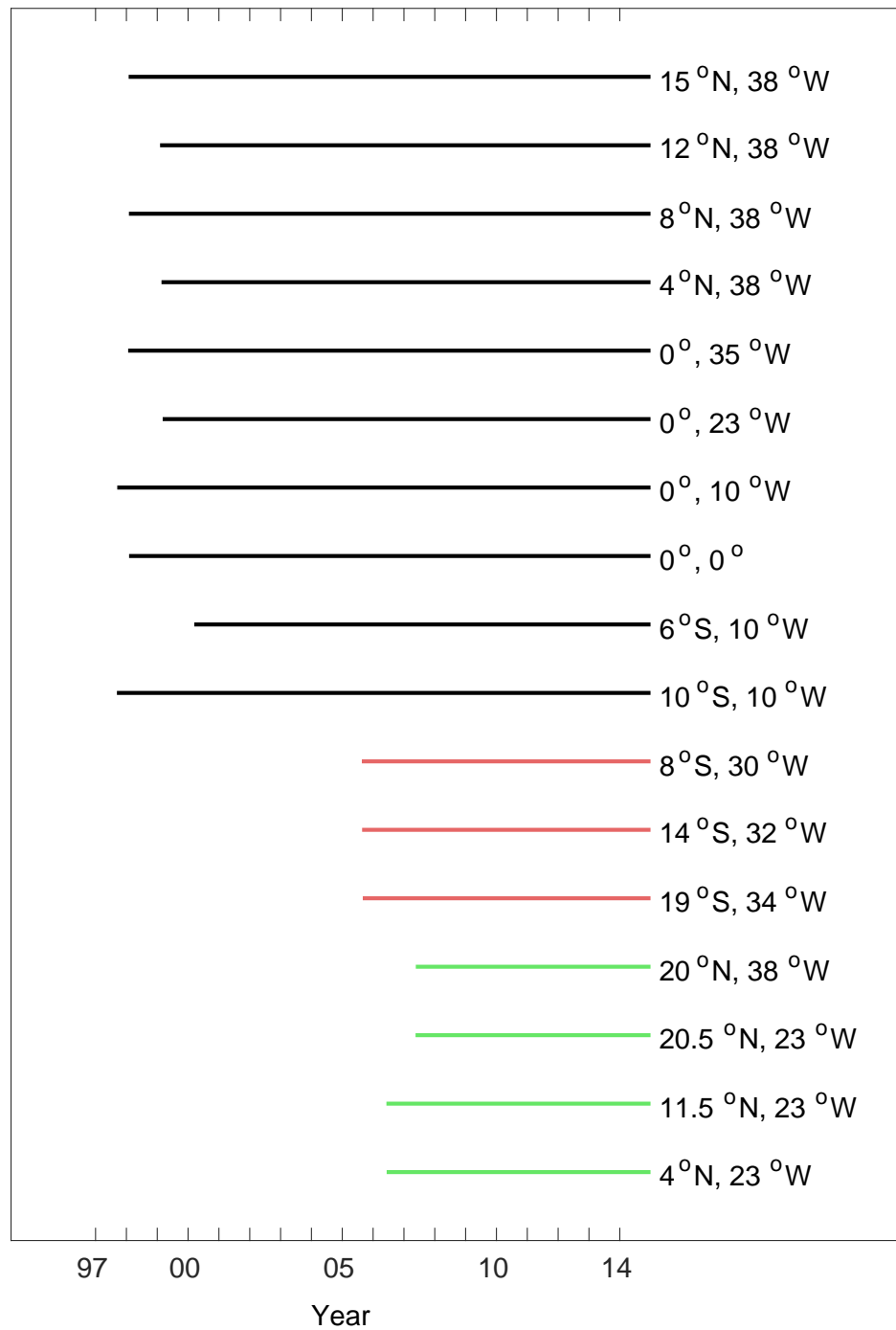


Figure 9 Availability of daily ePIRATA data at each mooring location. Black indicates “backbone” moorings, red shows Southwest Extension, and green Northeast Extension.

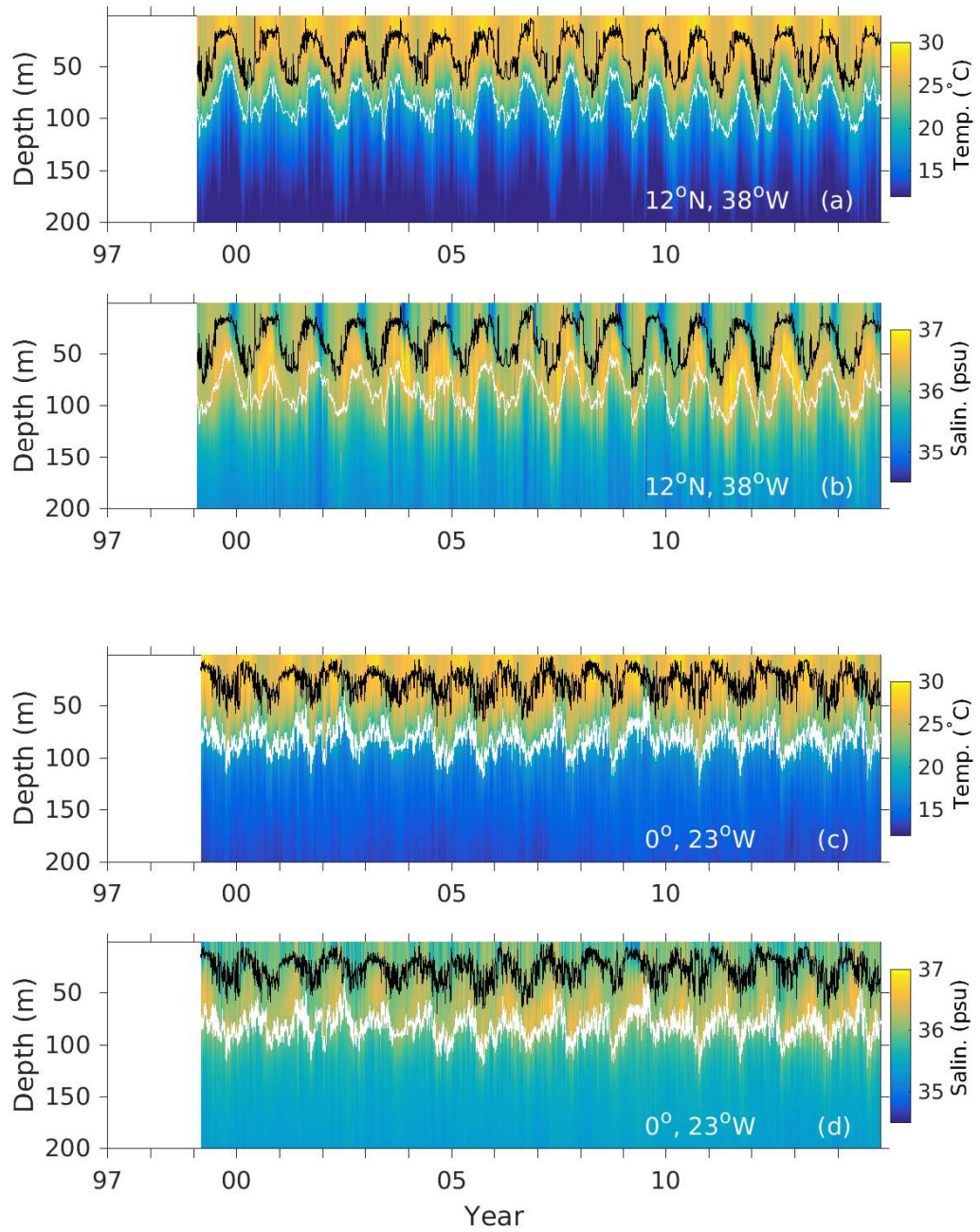


Figure 10 ePIRATA (a) temperature (shaded), mixed layer depth (black line), and depth of the 20°C isotherm (white line) at 12°N, 38°W. (b) Same as (a) except shading is salinity. (c) and (d) Same as (a) and (b) except at 0°, 23°W.

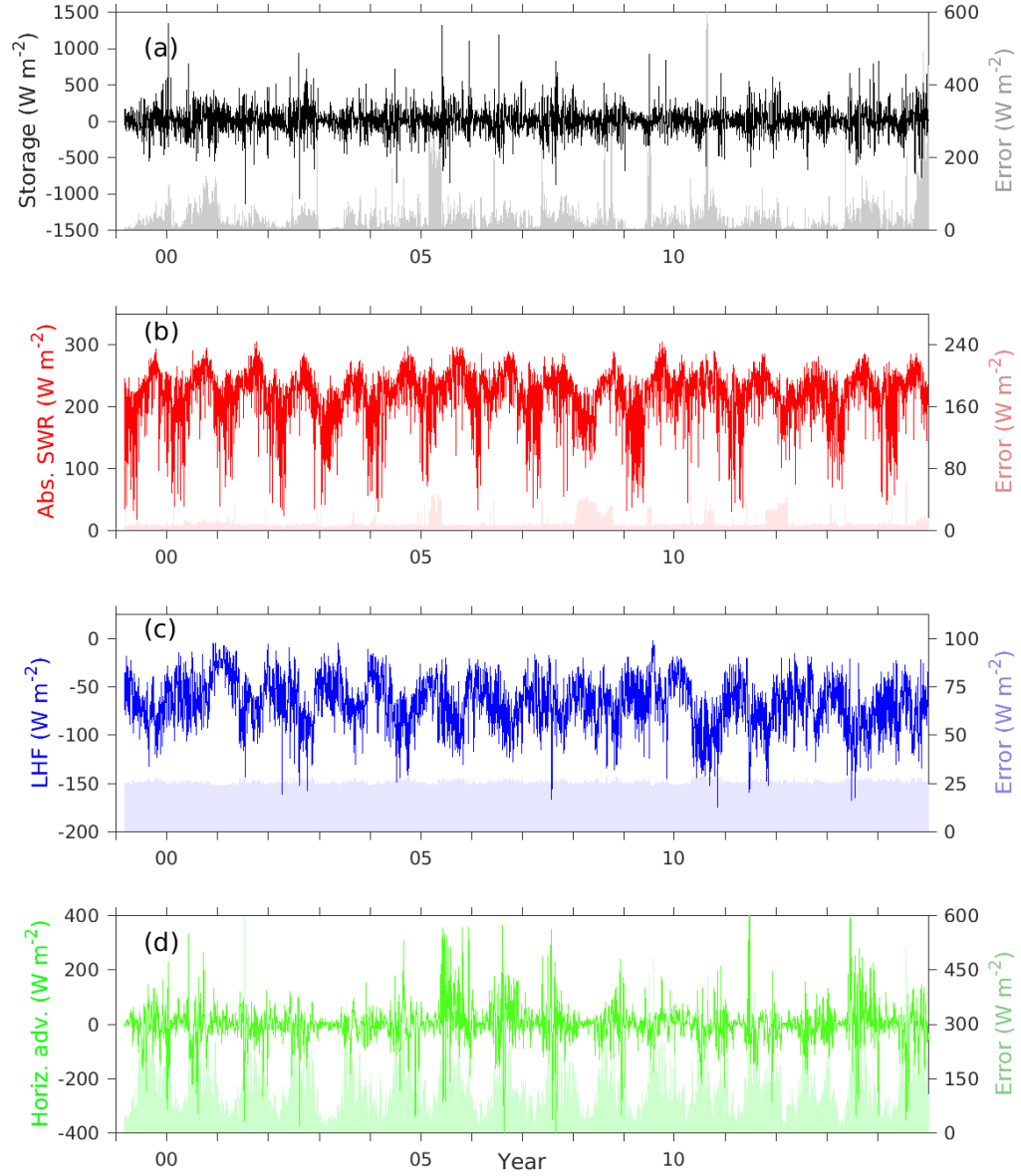


Figure 11 ePIRATA data at 0° , 23°W : (a) mixed layer heat storage rate (black line), (b) shortwave radiation absorbed in the mixed layer (red line), (c) latent heat flux (blue line), and (d) horizontal mixed layer heat advection (green line). In (a)-(d) shading indicates error estimates, with values on the right axis.

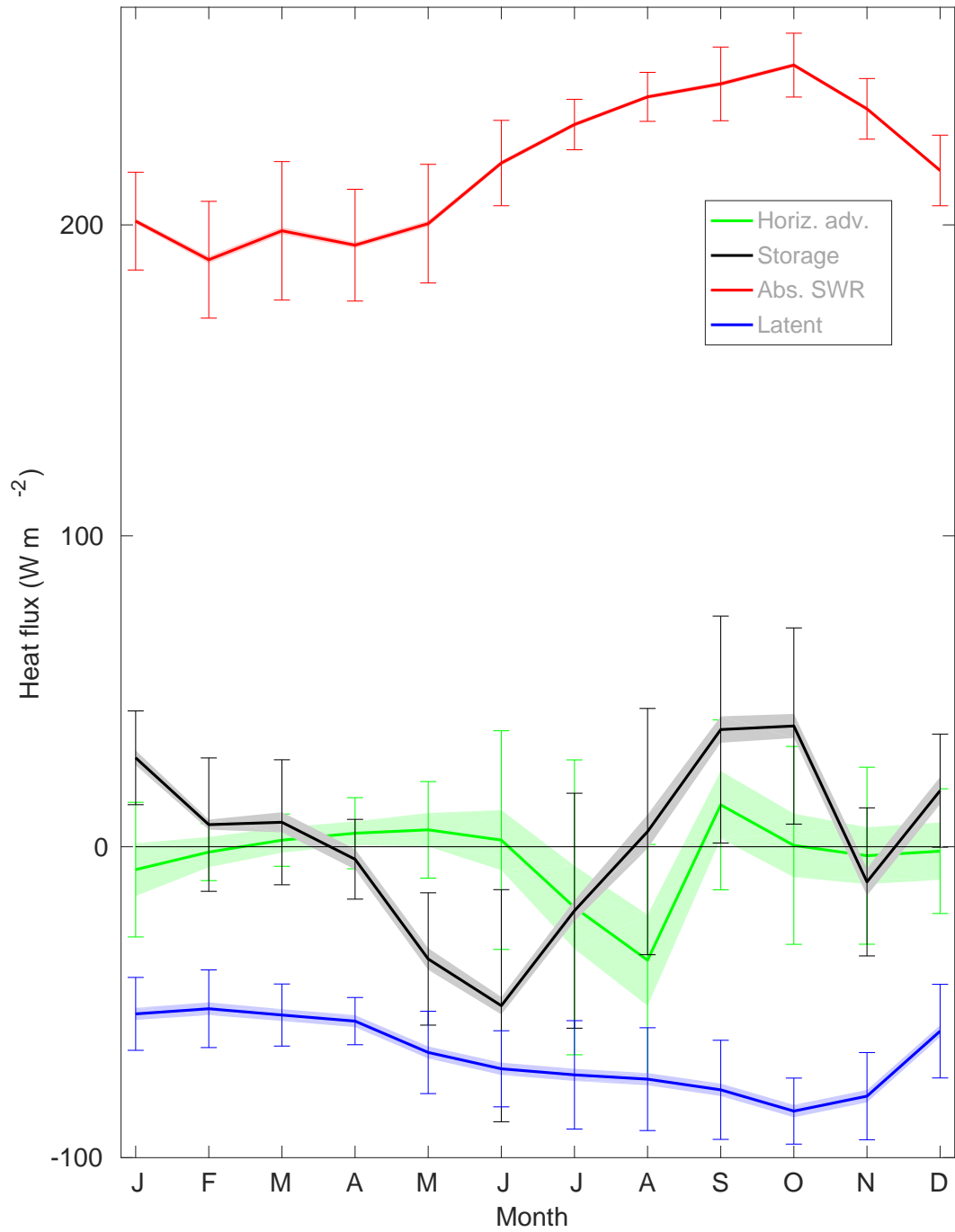


Figure 12 ePIRATA monthly mean climatological heat budget terms at 0°, 23°W: mixed layer heat storage rate (black line), (b) shortwave radiation absorbed in the mixed layer (red line), (c) latent heat flux (blue line), and (d) horizontal mixed layer heat advection (green line). Shading indicates error estimates and vertical error bars show the standard deviation for each calendar month across all years (a measure of interannual variability).

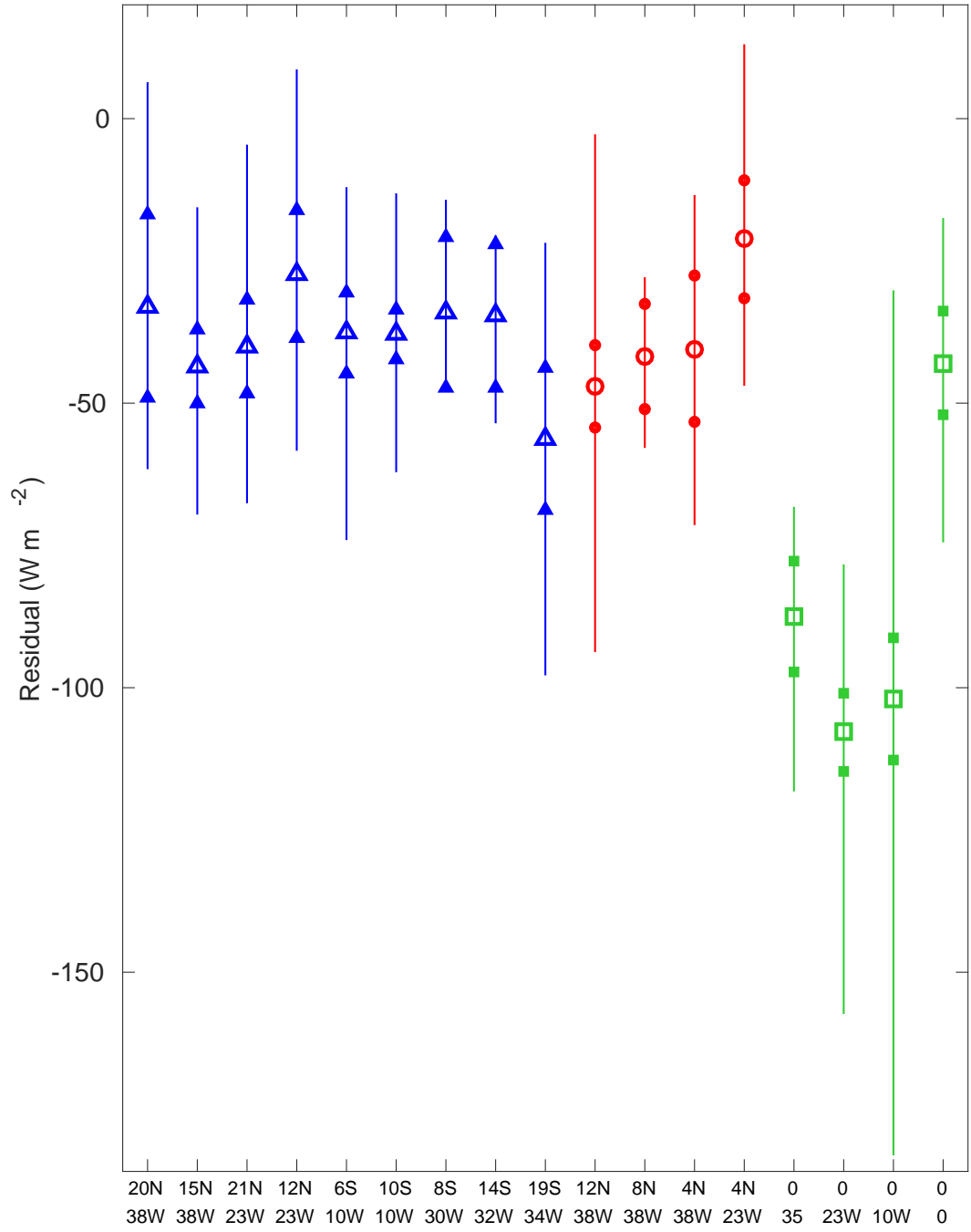


Figure 13 Heat budget residual (heat storage rate minus sum of net surface heat flux and horizontal advection) at each ePIRATA location. Large symbols represent record-length mean, lines show the range of climatological monthly values, and small symbols are the error estimates for the annual mean. Blue indicates locations outside of the ITCZ and equatorial regions, red shows locations in the ITCZ region, and green is for locations on the equator.

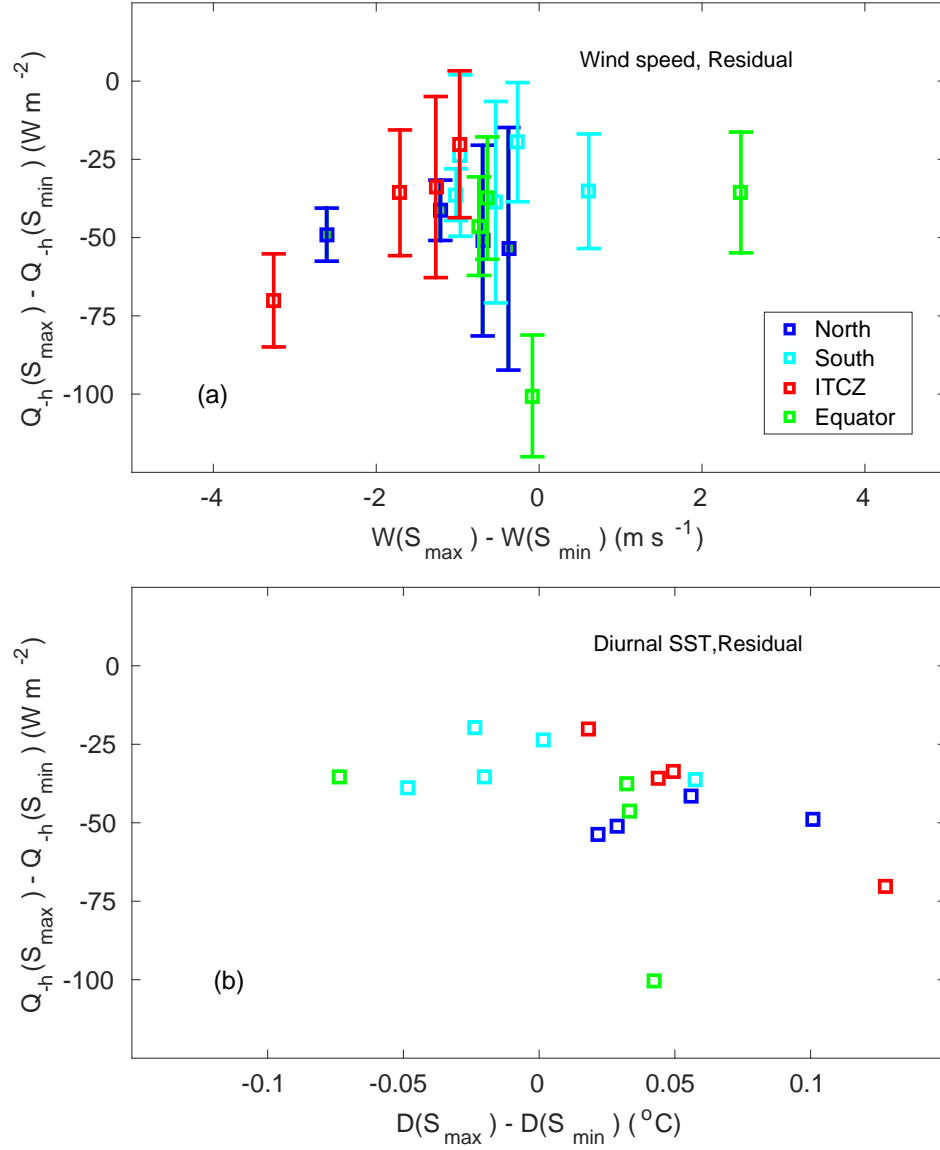


Figure 14 Scatter-plots of the seasonal range of Q_{-h} at each ePIRATA location, calculated as the difference between the three-month season (S_{max}) with the largest mean cooling from Q_{-h} (i.e., most negative value) and the three-month season (S_{min}) with the smallest cooling, versus (a) the corresponding wind speed difference, $W(S_{max}) - W(S_{min})$, and (b) the difference in the diurnal amplitude of SST. Dark blue and light blue indicate locations in the Northern and Southern Hemisphere, respectively, and outside of the ITCZ. Red indicates locations within the ITCZ, and green is for locations on the equator. Bars in (a) represent error estimates for each seasonal difference of Q_{-h} . Error bars for wind speed in (a) and SST in (b) are less than 0.1 m s^{-1} and 0.01°C , respectively, and are not shown.